J. Fluid Mech. (2005), *vol.* 536, *pp.* 155–184. © 2005 Cambridge University Press
doi:10.1017/S0022112005005008 Printed in the United Kingdom

Steady advection–diffusion around finite absorbers in two-dimensional potential flows

By JAEHYUK CHOI[1], DIONISIOS MARGETIS[1], TODD M. SQUIRES[2] AND MARTIN Z. BAZANT[1]

[1]Department of Mathematics, Massachusetts Institute of Technology, Cambridge, MA 02139, USA
[2]Departments of Applied and Computational Mathematics and Physics, California Institute of Technology, Pasadena, CA 91125, USA

(Received 22 March 2004 and in revised form 19 January 2005)

We consider perhaps the simplest non-trivial problem in advection–diffusion – a finite absorber of arbitrary cross-section in a steady two-dimensional potential flow of concentrated fluid. This problem has been studied extensively in the theory of solidification from a flowing melt, and it also arises in advection–diffusion-limited aggregation. In both cases, the fundamental object is the flux to a circular disk, obtained by conformal mapping from more complicated shapes. Here, we construct an accurate numerical solution by an efficient method that involves mapping to the interior of the disk and using a spectral method in polar coordinates. The method combines exact asymptotics and an adaptive mesh to handle boundary layers. Starting from a well-known integral equation in streamline coordinates, we also derive high-order asymptotic expansions for high and low Péclet numbers (*Pe*). Remarkably, the 'high'-*Pe* expansion remains accurate even for such low *Pe* as 10^{-3}. The two expansions overlap well near $Pe = 0.1$, allowing the construction of an analytical connection formula that is uniformly accurate for all *Pe* and angles on the disk with a maximum relative error of 1.75 %. We also obtain an analytical formula for the Nusselt number (*Nu*) as a function of *Pe* with a maximum relative error of 0.53 % for all possible geometries after conformal mapping. Considering the concentration disturbance around a disk, we find that the crossover from a diffusive cloud (at low *Pe*) to an advective wake (at high *Pe*) occurs at $Pe \approx 60$.

1. Introduction

The transfer of mass, heat, or other passive scalars in fluid flows is a major theme in transport science (Leal 1992). The canonical model problem involves a uniform background flow of speed, U_∞, and concentration, C_∞, past an absorbing object of characteristic size, L. Given the steady, incompressible flow field, $\boldsymbol{u}$ (scaled to U_∞), the steady tracer concentration around the object, c (scaled to C_∞), satisfies the (dimensionless) linear advection–diffusion equation,

$$Pe_o \boldsymbol{u} \cdot \nabla c = \nabla^2 c, \tag{1.1}$$

where $Pe_o = U_\infty L/D$ is the *bare* Péclet number, which measures the relative importance of advection compared to diffusion (with a diffusivity D). The partial differential equation (PDE) (1.1) must be solved subject to the boundary conditions (BCs) $c = 0$ on the object and $c = 1$ far away (at ∞), to obtain the dimensionless normal

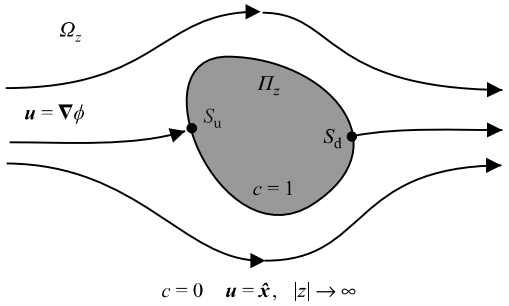

FIGURE 1. The fundamental problem of advection–diffusion: a finite absorber (source) in a steady flow of uniformly concentrated (depleted) fluid in the complex z-plane; Ω_z is the region exterior to the object.

flux density,

$$\sigma = \hat{\boldsymbol{n}} \cdot \nabla c, \tag{1.2}$$

everywhere on the surface of the object. (Since the problem is linear, we may also consider the equivalent problem of a source object at $c = 1$ relative to a depleted background fluid at $c = 0$.)

Although similarity solutions exist for infinite leading edges (see below), in the usual case of a *finite* absorber, the mathematical problem is intractable. It can even be difficult to solve numerically because Pe_o appears as a singular perturbation in the PDE in both limits, $Pe_o \to \infty$ and $Pe_o \to 0$. The classical approach, therefore, has been to employ asymptotic analysis to obtain approximate solutions, usually relating the total integrated flux, or Nusselt number, Nu, to the Péclet number, Pe. Early studies of this type focused on spheres (Acrivos & Taylor 1962) and more complicated shapes (Brenner 1963) in Stokes flows, and later studies dealt with heat or mass transfer in steady shear flow (Phillips 1990). Related work continues to the present day, e.g. in the context of nutrient uptake by single-cell organisms (Magar, Goto & Pedley 2003).

The $Nu(Pe)$ relation contains useful global information, but one sometimes requires a complete solution to the problem, including the local flux profile on the absorber. In this paper, we focus on a well-known special case, ideally suited for mathematical analysis and physical interpretation: steady advection–diffusion in a two-dimensional irrotational flow. The velocity field is described by the flow potential, ϕ, as $\boldsymbol{u} = \nabla\phi$ and the dimensionless boundary-value problem (BVP) is

$$Pe_o \nabla\phi \cdot \nabla c = \nabla^2 c, \quad \nabla^2\phi = 0, \quad (x, y) \in \Omega_z, \tag{1.3}$$

$$c = 1, \quad \hat{\boldsymbol{n}} \cdot \nabla\phi = 0, \quad (x, y) \in \partial\Omega_z \quad \text{and} \quad c \to 0, \quad x^2 + y^2 \to \infty; \tag{1.4}$$

$$\nabla\phi \to \hat{\boldsymbol{x}}, \quad x^2 + y^2 \to \infty, \tag{1.5}$$

where Ω_z is the flow region, exterior to the object's boundary, $\partial\Omega_z$, as shown in figure 1. Note that in (1.4) we use boundary conditions for desorption ($c = 1$ on the object and $c = 0$ far away), which are somewhat more convenient that those of adsorption ($c = 0$ on the object and $c = 1$ far away). The two problems are mathematically equivalent by linearity.

The key to analysing (1.3) is to view points in the plane as complex numbers, $z = x + \mathrm{i}y$. For example, this enables a transformation to streamline coordinates, $\Phi = \phi + \mathrm{i}\psi$, which reduces the problem to a thin absorbing strip in a uniform flow

(Boussinesq 1905). For a more general perspective in terms of conformal mapping, see Bazant (2004). Using complex-variable techniques, the general system of PDEs (1.3) has been studied recently with applications to tracer dispersion (Koplik, Redner & Hinch 1994) and heat transfer (Morega & Bejan 1994) in porous media, as well as vorticity diffusion in strained wakes (Eames & Bush 1999; Hunt & Eames 2002).

Complex analysis becomes particularly useful when the interface, $\partial\Omega_z(t)$, is a moving free boundary, driven by the local flux density, σ_z. For a broad class of transport-limited growth phenomena, the interfacial dynamics, whether deterministic or stochastic, can be formulated in terms of a time-dependent conformal map from a simple static domain to the evolving physical domain (Bazant, Choi & Davidovitch 2003). For continuous growth by advection–diffusion, this approach was introduced by van Wijngaarden (1966) and Maksimov (1976), who solved (1.3)–(1.5) in streamline coordinates. Maksimov's method has been used extensively by Kornev and his collaborators to describe solidification and freezing from a flowing melt (Chugunov & Kornev 1986; Kornev & Chugunov 1988; Kornev & Mukhamadullina 1994; Alimov, Kornev & Mukhamadullina 1994, 1998; Cummings & Kornev 1999; Cummings *et al.* 1999). These studies significantly extend the conformal-map dynamics for Laplacian growth by pure diffusion, without advection (Polubarinova-Kochina 1945; Galin 1945; Howison 1992).

Here, we are motivated by a new, discrete growth model, Advection–Diffusion-Limited Aggregation (ADLA), which describes the growth of fractal aggregates in a fluid flow via a stochastic conformal map (Bazant *et al.* 2003). In that case, the BVP (1.3)–(1.5) must be solved for a circular absorber for all values of Pe_o. The normal flux distribution, σ_z, determines the probability measure for growth events. The detailed description of the growth measure in this paper shows how the dynamics crosses over from diffusion-dominated to advection-dominated growth regimes, as a function of the time-dependent Péclet number. These two 'fixed points' of the dynamics are related to special similarity solutions (Bazant 2004), which correspond to the asymptotic regimes of high and low Pe_o analysed in this paper.

Beyond such applications, the BVP (1.3)–(1.5), for an arbitrary single-connected domain, Ω_z, merits serious mathematical study in its own right. It is perhaps the simplest advection–diffusion problem with a non-trivial dependence on the Péclet number. It may also be the most complicated advection–diffusion problem for which a nearly exact analytical solution is possible, as we show here.

The paper is organized as follows. In § 2 we set the stage for our analysis by reviewing two key properties of the BVP (1.3)–(1.5): (i) it can be recast as a singular integral equation in streamline coordinates, and (ii) conformal mapping can be applied to work in other convenient geometries for numerical solution and mathematical analysis. In § 3, we present an efficient new numerical method to solve the BVP, after conformal mapping to the interior of a circular disk. In § 4, we derive accurate asymptotic expansions for σ for high Péclet numbers by applying an exact iterative procedure to the integral equation. In § 5 approximate formulae for σ are derived when Pe is sufficiently small via approximating the kernel of the integral equation and solving the resulting equation exactly by known methods. In § 6 an accurate *ad hoc* connection formula is given for σ by combining the formulae for high and low Pe, and it is also integrated to obtain the $Nu(Pe)$ relation. Finally, in § 7 we conclude with a discussion of some of the implications and applications of our results, as well as by posing a few challenges for future work.

The computer programming codes used for the results in this paper are available at http://www.advection-diffusion.net.

2. Mathematical preliminaries

2.1. *Streamline coordinates*

In his analysis of high Reynolds number flows, Boussinesq (1905) discovered a hodograph transformation (exchanging dependent and independent variables) which greatly simplifies (1.3). It is well known that the velocity potential is the real part of an analytic complex potential, $\Phi = \phi + \mathrm{i}\psi$, where the harmonic conjugate, ψ, is the stream function (Batchelor 1967). Using the Cauchy–Riemann equations, it is easy to show that the concentration profile, c, satisfies the simplified PDE

$$Pe_o \frac{\partial c}{\partial \phi} = \frac{\partial^2 c}{\partial \phi^2} + \frac{\partial^2 c}{\partial \psi^2}, \tag{2.1}$$

in 'streamline coordinates', (ϕ, ψ). The physical significance of this equation is that advection (the left-hand side) only occurs along streamlines, while diffusion (the right-hand side) also occurs in the transverse direction, along isopotential lines.

Boussinesq's transformation corresponds to a conformal mapping to a plane of a uniform flow, described by a constant $\nabla\phi$. Therefore, an arbitrary domain, Ω_z, as shown in figure 1, is mapped to the exterior of a straight line segment, or strip, parallel to the streamlines (which is a branch cut of the inverse map). Some examples are given in figure 2. In streamline coordinates, the BCs (1.4) and (1.5) are transformed as follows:

$$c = 1, \quad \psi = 0, \ -2A < \phi < 2A, \quad \text{and} \quad c \to 0 \quad \text{as } \phi^2 + \psi^2 \to \infty. \tag{2.2}$$

The constant A is determined so that $4A$ is equal to the difference of the flow potential ϕ between two stagnant points, for example, the points $\mathrm{S_u}$ and $\mathrm{S_d}$ shown in figure 1.

2.2. *Formulation as an integral equation*

In streamline coordinates, the advection–diffusion process past a finite strip can be formulated in terms of an integral equation using the classical method of Green's functions (Stakgold 1998). For reasons to become clear in § 2.3, we let $x = \phi$, $y = \psi$, $A = 1/2$, and $Pe = Pe_o/2$, so the BVP (2.1)–(2.2) takes the form

$$2Pe \frac{\partial c}{\partial x} = \frac{\partial^2 c}{\partial x^2} + \frac{\partial^2 c}{\partial y^2}, \tag{2.3}$$

$$c = 1 \quad \text{on } y = 0, \ -1 < x < 1 \quad \text{and} \quad c = 0 \quad \text{as } x^2 + y^2 \to \infty. \tag{2.4}$$

Green's function $G(x, y)$ for (2.3) and (2.4), which expresses the concentration profile generated by a unit source flux at the origin, satisfies the PDE

$$2Pe \frac{\partial G}{\partial x} - \frac{\partial^2 G}{\partial x^2} - \frac{\partial^2 G}{\partial y^2} = \delta(x)\delta(y).$$

After removing the first derivative term by a change of variables and using polar coordinates,

$$G(x, y) = \mathrm{e}^{Pe\, x} F(r, \theta), \tag{2.5}$$

we find that F obeys the Helmholtz equation

$$\nabla^2 F - Pe^2 F = \delta(x)\delta(y), \tag{2.6}$$

whose solution is a modified Bessel function of the second kind, $K_0(Per)$, where $r = (x^2 + y^2)^{1/2}$. Taking into account the unit normalization, we obtain Green's function,

$$G(x, y) = \mathrm{e}^{Pe\, x} K_0(Per)/2\pi. \tag{2.7}$$

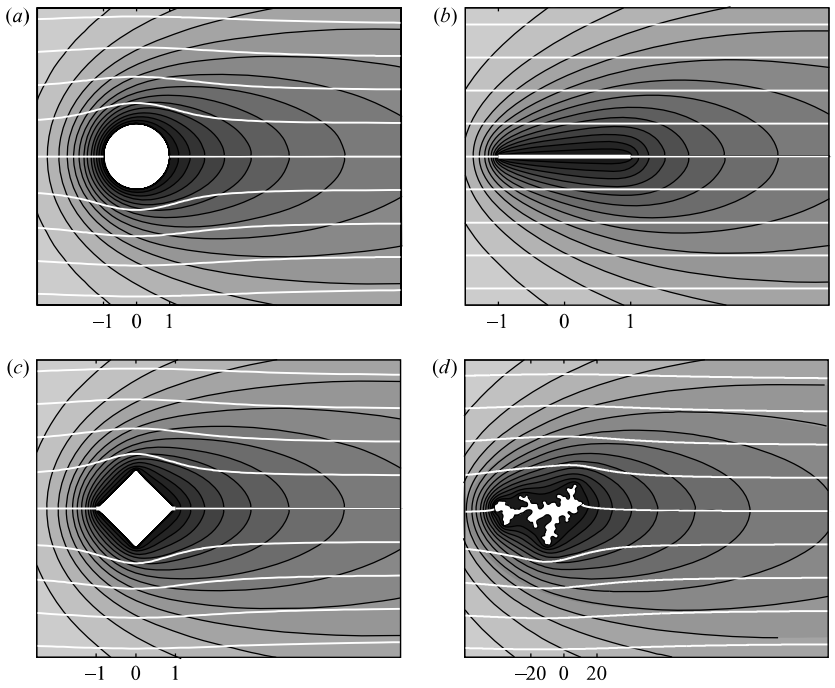

FIGURE 2. Numerical solutions using the method of § 3 for the concentration profile (contour plot) and streamlines (open curves) around different absorbing objects in a uniform background potential flow: (*a*) the unit disk, (*b*) a finite strip, (*c*) a square, and (*d*) an ADLA fractal cluster with $Pe_o = 1, 2, 1.2$ and 0.05 respectively. The geometries in (*b*), (*c*) and (*d*) are obtained by conformal mapping from (*a*). Case (*b*) corresponds to streamline coordinates; case (*c*) is obtained by the numerical Schwartz–Christoffel mapping (Trefethen 1986); case (*d*) is obtained from a stochastic, iterated conformal map (Bazant *et al.* 2003). The horizontal axis is labelled by numerical values of the spatial coordinate x. However, the distances in the figures (*a*)–(*d*) are scaled by the 'conformal radius' A_1, see (2.11) below, which is the characteristic size of the physical object. The A_1 is chosen so that the renormalized Péclet number is the same, $Pe = A_1 Pe_o = 1$, in all cases, which explains why the far-field solutions look the same.

The concentration profile, c, everywhere in streamline coordinates is obtained by convolving Green's function, G, with the flux on the strip,

$$c(x, y) = \int_{-1}^{1} G(x - x', y) 2\sigma(x')\,\mathrm{d}x', \tag{2.8}$$

where the factor 2 is included because the flux has the same value,

$$\sigma(x) = -\frac{\partial c}{\partial y}(x, 0^+) = \frac{\partial c}{\partial y}(x, 0^-),$$

on the upper and the lower sides of the strip, respectively. Therefore, the boundary value problem described by (2.3) and (2.4) is equivalent to finding the $\sigma(x)$ that satisfies the integral equation (Pearson 1957; van Wijngaarden 1966)

$$\int_{-1}^{1} \mathrm{e}^{Pe(x-x')} K_0(Pe|x - x'|)\sigma(x')\,\mathrm{d}x' = \pi, \quad -1 < x < 1, \tag{2.9}$$

which forms the basis for the theory of solidification in flowing melts (Maksimov 1976). In this context, (2.9) has been analysed for large and small Pe by Kornev and collaborators, as cited in the introduction. Below, we will extend these results and construct an analytical approximation that is uniformly accurate in both Pe and x.

The reader may worry about the existence and uniqueness of solutions because (2.9) is a Fredholm-type equation of the first kind (with a difference kernel). In the present case, however, the symmetrized kernel, $K_0(Pe|x-x'|)$, is positive definite, and thus invertible; see the Appendix for an explanation.

It seems tempting to approach (2.9) using Fourier-type methods because it involves a convolution (Titchmarsh 1948), but the kernel is not a periodic function. We also note that the kernel is singular and not of the classical Cauchy type (Muskhelishvili 1992). It is known that (2.9) admits a solution which can be expanded in terms of Mathieu functions (Rvachev 1956; Protsenko & Rvachev 1976), but such representations are impractical for computations over a wide range of Pe, and give no insight into the dependence of the flux σ on x and Pe. The collocation method has been used successfully to obtain numerically the solution of (2.9) (Kornev & Mukhamadullina 1994).

2.3. *The general principle of conformal invariance*

There is a simple way to understand why Boussinesq's transformation works: the advection–diffusion PDE (1.3) is invariant under conformal changes of variables, even though its solutions are not harmonic functions, which also holds more generally for some other equations (Bazant 2004). As such, the boundary value can be transformed to any convenient geometry by conformal mapping. Streamline coordinates is a good choice for asymptotics, but other choices are better suited for numerical analysis and similarity solutions.

Here, we exploit this general principle to map the BVP (1.3)–(1.5) to other useful coordinate systems. If $\phi_w = \mathrm{Re}\,\Phi(w)$ and $c_w = F(w, \overline{w})$ (where $\overline{w}$ denotes the complex conjugate of w) solve (1.3) in some simple domain, Ω_w, then $\phi_z = \mathrm{Re}\,\Phi(f(z))$ and $c_z = F(f(z), \overline{f(z)})$ solve (1.3) in an arbitrary mapped domain, $\Omega_z = g(\Omega_z)$, where $z = g(w) = f^{-1}(w)$. The concentration BCs (1.4) are conformally invariant, but, since the BC (1.5) prescribing the background flow is not, due to the gradient, care must be taken in transforming the solution.

For advection–diffusion-limited growth (Bazant *et al.* 2003), it is natural to let Ω_w be the exterior of the unit circle, so our canonical problem is that of a concentrated flow past a circular absorber, shown in figure 2(*a*), with the velocity potential

$$\phi = \mathrm{Re}\left\{w + \frac{1}{w}\right\}, \quad |w| > 1. \tag{2.10}$$

To reach other geometries, the mapping, $z = g(w)$, must be univalent (conformal and one-to-one), so it has a Laurent series of the form

$$g(w) = A_1 w + A_0 + \frac{A_{-1}}{w} + \cdots, \quad |w| > 1, \tag{2.11}$$

where A_1 is a positive real constant which defines an effective diameter of Ω_z (the 'conformal radius'). In order to preserve the BC (1.5) which sets a unit flow speed at $z = \infty$, we would need to set the dimensionless flow speed to A_1 at $w = \infty$. Instead, we choose to redefine the velocity potential in Ω_w to preserve the unit flow speed, as in (2.10), and then define a *renormalized* Péclet number, $Pe = A_1\, Pe_o$, analogous to the time-dependent Péclet number for ADLA defined by Bazant *et al.* (2003).

The BVP for the concentration Ω_w then becomes

$$Pe\nabla\phi\cdot\nabla c = \nabla^2 c, \quad |w|>1, \tag{2.12}$$

$$c=1 \quad \text{on } |w|=1, \quad \text{and} \quad c=0 \quad \text{as } |w|\to\infty. \tag{2.13}$$

The physical significance of the renormalized Péclet number, Pe, is that it determines the far-field solution, independent of the absorber's shape and the bare Péclet number. This point is illustrated in figure 2, where the concentration and flow field far away from various objects at $Pe=1$ look the same, in spite of extremely different shapes, ranging from a circle to a fractal ADLA cluster. Therefore, we view Pe as the basic parameter in our analysis, from which we define the bare Péclet number, $Pe_o = Pe/A_1$, for arbitrary domains, in terms of the univalent map from the exterior of the unit circle.

From this perspective, streamline coordinates are obtained via the Joukowski transformation (Carrier, Krook & Pearson 1983) $g(w)=(w+1/w)/2$, which maps the unit circular disk onto the finite strip of length 2 centred at the origin along the real axis. The BVP (2.12)–(2.13) is then transformed to the form (2.3)–(2.4) given above. In general, the fluxes on the boundaries $\partial\Omega_z$ (the absorber surface) and $\partial\Omega_w$ (the unit circle, $w=\mathrm{e}^{\mathrm{i}\theta}$) are related by

$$\sigma_w(\theta;Pe) = |g'(w)|\,\sigma_z(g(w);Pe), \tag{2.14}$$

where σ_w is the flux on $\partial\Omega_w$ and σ_z is the flux on $\partial\Omega_z$. In the case of streamline coordinates (2.3)–(2.4), the flux on the strip, $\sigma_z(x;Pe)$, is thus related to the flux on the circle, $\sigma_w(\theta;Pe)$, by

$$\sigma_w(\theta;Pe) = |\sin\theta|\,\sigma_z(\cos\theta;Pe). \tag{2.15}$$

For a bounded flux on the circle, σ_w, the flux on the strip, σ_z, always diverges as $O[(1-x^2)^{-1/2}]$ as x approaches ±1. Therefore, although we will use the strip geometry, Ω_z, for asymptotic analysis in §§4 and 5, the circle geometry, Ω_w, is a better starting point for our numerical analysis in §3. In all cases, however, our goal is to obtain the flux on the circle, the canonical geometry for a finite absorber.

2.4. *Similarity solutions for semi-infinite leading edges*

Before proceeding with our analysis, we mention a class of similarity solutions for 'leading edges' which have relevance for the high-Pe limit of our problem. For this section only, we use the upper half-plane, $\{\mathrm{Im}\,w>0\}$, as our simple domain, Ω_w. For a straining velocity field, $\phi(w)=\mathrm{Re}\,w^2$, bringing fluid toward the plane, there is a classical similarity solution for the concentration profile, $c(w,\overline{w})=\mathrm{erfc}(\sqrt{Pe_o}\,\mathrm{Im}\,w)$, for which the flux on the real axis is a constant, $\sigma_w=2\sqrt{Pe_o/\pi}$. (As usual, the complementary error function is defined by $\mathrm{erfc}(z)=(2/\sqrt{\pi})\int_z^\infty \mathrm{d}t\,\mathrm{e}^{-t^2}$.)

For every conformal map, $w=f(z)$, from the z-plane to the upper half-w-plane, there corresponds another similarity solution (Cummings *et al.* 1999; Bazant 2004),

$$\phi = \mathrm{Re}\,f(z)^2 \quad \text{and} \quad c=\mathrm{erfc}(\sqrt{Pe_o}\,\mathrm{Im}\,f(z)) \quad \text{for } \mathrm{Im}\,w\geqslant 0. \tag{2.16}$$

Note that the boundary condition $\nabla\phi\sim\hat{\boldsymbol{x}}$ as $|z|\to\infty$ holds only if $f(z)\sim\sqrt{z}$ as $|z|\to\infty$, so these solutions correspond to more general flows near stagnation points. For the purposes of this paper, we discuss two choices for $f(z)$:

(*a*) $f(z)=\sqrt{z}$, which maps the entire z-plane, with the exception of the branch cut $\{\mathrm{Im}\,z=0,\ \mathrm{Re}\,z>0\}$, onto Ω_w. The (x,y) coordinates of the z-plane then correspond to the streamline coordinates, and the flux on the strip is $\sigma(x)=\sqrt{Pe_o/\pi x}$. This well-known formula can also be derived via replacing the upper limit of integration in

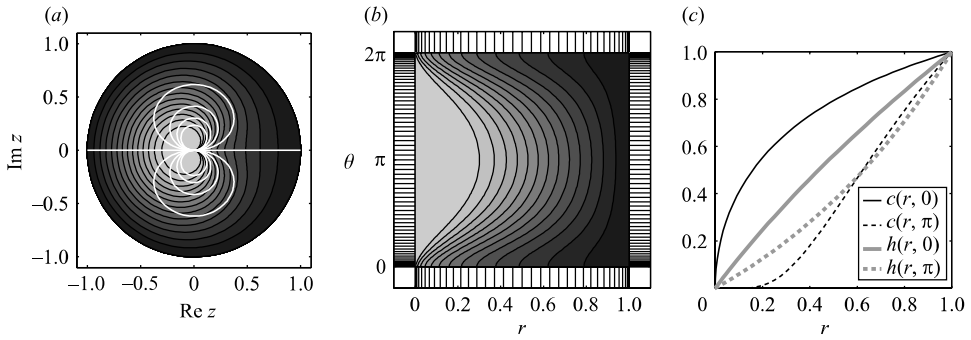

FIGURE 3. The concentration profile ($Pe = 1$) calculated numerically in the interior of the circular disk is shown (a) in Cartesian coordinates, and (b) in polar coordinates. In (c) the numerically obtained values are shown for $c(r, \theta = 0)$ (thin solid line), $c(r, \theta = \pi)$ (thin dashed line), $h(r, \theta = 0)$ (thick solid line), and $h(r, \theta = \pi)$ (thick dashed line).

(2.9) by ∞, and applying the Wiener–Hopf method of factorization (Krein 1962; van Wijngaarden 1966; Carrier *et al.* 1983). This procedure is carried out systematically to all orders of approximation in § 4 and via a different, rigorous method by Margetis & Choi (2004).

(b) $f(z) = \sqrt{z} + 1/\sqrt{z}$, which maps the exterior of the circular rim, $\{z : |z| > 1$ and $0 < \arg z < 2\pi\}$, onto Ω_w (Bazant 2004). This solution describes the advection-dominated (high-Pe) fixed point of the ADLA fractal-growth process (Bazant *et al.* 2003). From (2.16) with $z = re^{i\theta}$ and $r \geqslant 1$, we find

$$c(r, \theta) = \operatorname{erfc}\left[\sqrt{Pe_o}\left(\sqrt{r} + \frac{1}{\sqrt{r}}\right)\sin\left(\frac{\theta}{2}\right)\right], \quad \sigma(\theta) = 2\sqrt{\frac{Pe_o}{\pi}}\sin\left(\frac{\theta}{2}\right), \tag{2.17}$$

which is the leading-order solution for our BVP (2.12)–(2.13) as $Pe_o = Pe \to \infty$.

The fact that we consider *finite* absorbers leads to significant analytical and numerical complications, which are the focus of this paper.

3. Numerical solution

3.1. *Conformal mapping to polar coordinates inside the unit disk*

In this section we determine the concentration profile c by numerically solving the BVP (2.12)–(2.13). One of the difficulties in applying a numerical method is related to the fact that the region Ω_w is unbounded. By invoking conformal invariance again, however, we can apply a transformation that leaves the BVP unchanged yet maps Ω_w to a bounded region. In particular, we use inversion, $g(w) = 1/w$, to map the disk exterior onto its interior. Physically, this corresponds to a dipole source of concentrated fluid inside an absorbing circular cylinder, as shown in figure 3(a). With $g(w) = re^{i\theta}$ the problem is expressed in the polar coordinates (r, θ) by

$$r^3\frac{\partial^2 c}{\partial r^2} + \{r^2 + Per(1 - r^2)\cos\theta\}\frac{\partial c}{\partial r} + r\frac{\partial^2 c}{\partial \theta^2} + Pe(1 + r^2)\sin\theta\frac{\partial c}{\partial \theta} = 0, \tag{3.1a}$$

$$c = 0 \quad \text{at } r = 0, \quad \text{and } c = 1 \quad \text{at } r = 1, \tag{3.1b}$$

where $r \leqslant 1$ and $0 \leqslant \theta < 2\pi$. A solution in the (r, θ)-plane is shown in figure 3(b).

3.2. *Analytical treatment of singularities*

Before we apply any numerical method to (3.1) directly, we note that the concentration profile c as a function of (r, θ) exhibits singular behaviour as r approaches 0. We first need to modify (3.1*a*) in order to eliminate this behaviour, which undermines the accuracy of our numerical method. From the similarity solution (2.17) and Green's function of § 2.2 we obtain the leading-order behaviour

$$c(r,\theta) = O\left\{\sqrt{r}\ \exp\left[Pe\left(2-\frac{1}{r}-r\right)\sin^2\left(\frac{\theta}{2}\right)\right]\right\} \quad \text{as } r \to 0. \tag{3.2}$$

First, the square-root limit $c(r, \theta = 0) = O(\sqrt{r})$ cannot be treated easily in numerical methods because of the resulting diverging derivative near $r = 0$. Second, the essential singularity at $r = 0$, $c(r, \theta = \pi) = O(\sqrt{r}\ \mathrm{e}^{-Pe/r})$, forces c to change drastically near $r = 0$. Especially when Pe is large, this limiting behaviour is extended even to $r < 1 - O(1/\sqrt{Pe})$. To avoid this behaviour, we define a function $h(r, \theta)$ by factoring out the leading-order singular behaviour of $c(r, \theta)$ as

$$\sqrt{r}\ \exp\left\{Pe\left(2-\frac{1}{r}-r\right)\sin^2\left(\frac{\theta}{2}\right)\right\}h(r,\theta) \equiv r\ c(r,\theta), \tag{3.3}$$

and apply the numerical method shown below directly to this $h(r, \theta)$. Note that the c is multiplied by r on the right-hand side of (3.3) to ensure that $h(r, \theta) = O(r)$ as $r \to 0$; thus, $h = 0$ at $r = 0$, which is the same condition as for c. Combining (3.1*a*) and (3.3) we obtain a PDE for $h(r, \theta)$:

$$r^3\frac{\partial^2 h}{\partial r^2} + Pe(r-r^3)\frac{\partial h}{\partial r} + r\frac{\partial^2 h}{\partial \theta^2} + 2Pe\, r\sin\theta\frac{\partial h}{\partial \theta} + \left\{Pe(r\cos\theta - 1) + \frac{r}{4}\right\}h = 0. \tag{3.4}$$

By comparison of (3.1*a*) and (3.4), we note that the coefficients of the derivatives are simplified in (3.4). Once h is determined from (3.4), c is simply recovered via (3.3), and $\sigma(\theta)$ is obtained as

$$\sigma(\theta) = \left.\frac{\partial c}{\partial r}\right|_{(r=1,\theta)} = \left.\frac{\partial h}{\partial r}\right|_{(r=1,\theta)} - \frac{1}{2}.$$

Figure 3(*c*) shows how the singular behaviour of c is mitigated by introducing the new variable h.

3.3. *Spectral method*

The numerical differentiations with respect to the variables r and θ are carried out by spectral methods (Trefethen 2000). The spatial nodes, the points (r_j, θ_k) where the function is evaluated numerically, are determined by

$$r_j = \frac{1}{2}\left(1-\cos\frac{j\pi}{N_r}\right) \quad \text{and} \quad \theta_k = \pi\left(1-\cos\frac{k\pi}{N_\theta}\right),$$

where $j = 1, \ldots, N_r$ and $k = 0, \ldots, N_\theta$; the nodes have higher density at the endpoints as shown in the frame around figure 3(*b*). Once the function values are given at the nodes, the derivatives at these points are calculated by interpolation via Chebyshev's polynomials. This procedure is very efficient, as the error in the spectral method is known to decrease exponentially in the number of nodes (Trefethen 2000). We used $N_r = 50$ and $N_\theta = 100$ (in practice $N_\theta = 50$ exploiting the symmetry in θ) for all the numerical results appearing in this paper.

Figure 4 shows the concentration profile, $c(r, \theta)$, for Pe of different orders of magnitude. As Pe increases, there is an apparent crossover from a diffusion-dominated

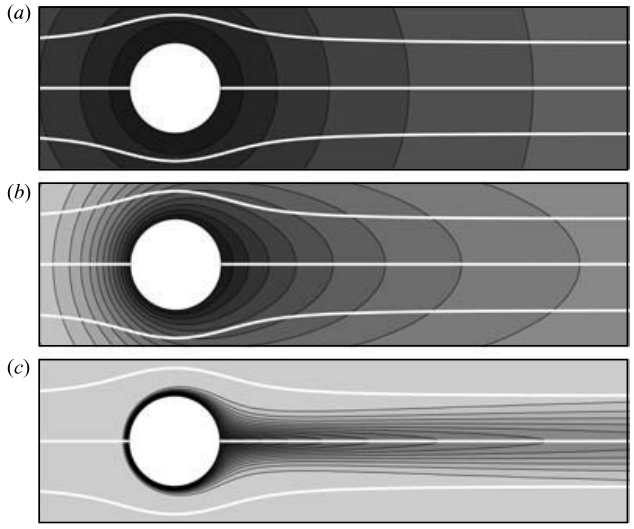

FIGURE 4. Concentration profiles for adsorption (or desorption) around the unit circular disk for (*a*) $Pe = 0.01$, (*b*) $Pe = 1$, and (*c*) $Pe = 100$.

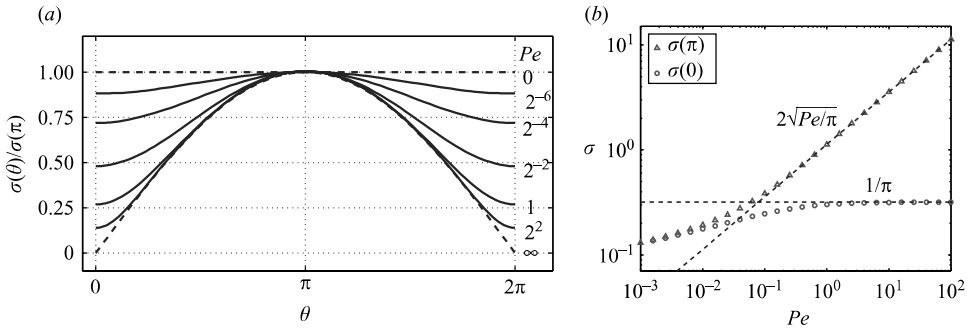

FIGURE 5. The flux $\sigma(\theta)$ is plotted around the unit disk for different values of Pe : (*a*)$\sigma(\theta)/\sigma(\pi)$ for $Pe = 0, 2^{-6}, 2^{-4}, 2^{-2}, 1, 2^2, \infty$, and (*b*) the values $\sigma(\theta = \pi)$ and $\sigma(\theta = 0)$ for a range of Pe.

regime (*a*), where the concentration disturbance looks like a 'cloud' extending in all directions, to an advection-dominated regime (*c*), where concentration gradients are confined to a narrow boundary layer which separates into a thin wake downstream. Understanding the crossover regime (*b*) to (*c*) is an important part of this paper, revisited below in § 7, following our analysis of the flux profile.

Figure 5 shows the flux density on the absorber, $\sigma(\theta)$, for different values of Pe. To check the validity of our numerical method, we compare the result for σ with the asymptotic expansion for high Pe from § 4 below, which can be numerically evaluated to any order. For this comparison we used the intermediate range of Péclet numbers $10^{-2} < Pe < 10^2$ for which the series converge fast enough yet the numerical method is stable. When $N_r = 50$ and $N_\theta = 100$ nodes are used for the discretization, the relative error measured as $\|\sigma_{\text{num}} - \sigma_{\text{asym}}\|/\|\sigma_{\text{asym}}\|$ is of the order of 10^{-5} or smaller; here, σ_{num} and σ_{asym} denote the numerical and the asymptotic solutions, respectively, and the norm is defined as $\|\sigma\| = \max\{\theta \in [0, 2\pi) : |\sigma(\theta)|\}$.

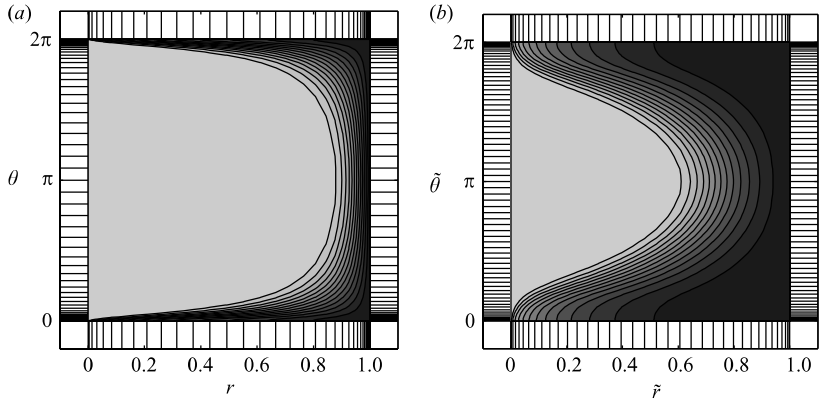

FIGURE 6. Contour plots of h for $Pe = 100$ (a) in the (r, θ)-plane, and (b) in the $(\tilde{r}, \tilde{\theta})$-plane.

If Pe lies outside the given intermediate range, care should be exercised in using our numerical method as explained in the next subsection. For such cases, however, the asymptotic, analytical formulae of §§4 and 5 give sufficently accurate solutions. The reader is referred to §§4 and 5 for details on the formulae and the comparisons with the numerical solution.

3.4. *Adaptive mesh for very high Péclet numbers*

A feature of the solution c that may undermine the accuracy of our numerics is the emergence of boundary layers for sufficiently large Pe. By virtue of (4.16) below we expect that for $Pe \gg 1$,

$$\left.\frac{\partial c}{\partial r}\right|_{(r=1,\theta)} = \sigma(\theta) = \begin{cases} 2\sqrt{Pe/\pi}\,\sin(\theta/2) & \text{when } \theta \gg O(1/\sqrt{Pe}) \\ 1/\pi & \text{when } \theta \leqslant O(1/\sqrt{Pe}). \end{cases} \tag{3.5}$$

So, $c(r, \theta)$ has boundary layers near $r = 1$ and $\theta = 0$, 2π whose widths are $O(1/\sqrt{Pe})$, as indicated in figure 6(a). The layer at $\theta = 0$ corresponds to the 'tail' shown in figure 4(c). Thus, the numerical method starts to break down when the node spacing becomes of the order of $1/\sqrt{Pe}$.

We next outline a technique to deal with the case of very high Pe within our numerical procedure. The idea is to introduce a set of independent variables, $\tilde{r} = \tilde{r}(r)$ and $\tilde{\theta} = \tilde{\theta}(\theta)$, so that c is a sufficiently smooth function of $\tilde{r}$ and $\tilde{\theta}$. The following conditions are required for $\tilde{r}(r)$ and $\tilde{\theta}(\theta)$:

$$\tilde{r}(0) = 0, \quad \tilde{r}(1) = 1, \quad \tilde{r}'(1) = O(\sqrt{Pe}), \tag{3.6}$$

$$\tilde{\theta}(0) = 0, \quad \tilde{\theta}(2\pi) = 2\pi, \quad \tilde{\theta}'(0) = O(\sqrt{Pe}), \tag{3.7}$$

where the prime here denotes differentiation with respect to the argument. Once $\tilde{r}(r)$ and $\tilde{\theta}(\theta)$ are defined, we find the PDE for $\tilde{h}(\tilde{r}, \tilde{\theta}) \equiv h(r(\tilde{r}), \theta(\tilde{\theta}))$ from (3.4) by applying the chain rule for the differentiations with respect to r and θ; for example,

$$\frac{\partial h}{\partial r} = \frac{1}{r'(\tilde{r})}\frac{\partial \tilde{h}}{\partial \tilde{r}}, \quad \frac{\partial^2 h}{\partial r^2} = \frac{1}{r'(\tilde{r})^2}\frac{\partial^2 \tilde{h}}{\partial \tilde{r}^2} - \frac{r'(\tilde{r})}{r'(\tilde{r})^3}\frac{\partial \tilde{h}}{\partial \tilde{r}}. \tag{3.8}$$

We solve the resulting PDE numerically. A convenient choice for $r(\tilde{r})$ and $\theta(\tilde{\theta})$ is

$$r(\tilde{r}) = \tilde{r} + \frac{1}{\pi}\left(1 - \frac{1}{\sqrt{Pe}}\right)\sin(\pi\tilde{r}), \quad \theta(\tilde{\theta}) = \tilde{\theta} - \left(1 - \frac{1}{\sqrt{Pe}}\right)\sin\tilde{\theta}. \tag{3.9}$$

The advantage of using $\tilde{r}$ and $\tilde{\theta}$ instead of r and θ is illustrated in figure 6 for $Pe = 100$. The effects of the boundary layers in (r, θ) are notably suppressed in the formulation using $(\tilde{r}, \tilde{\theta})$. In §§4 and 5 we discuss the high- and low-Pe asymptotics and their comparisons with the solution determined numerically by the method of this section.

4. Direct perturbation analysis for 'high' Péclet numbers

In this section, we derive an approximate analytical solution to the integral equation (2.9) in terms of series expansions produced via suitable iterations in the coordinate space. We also obtain closed-form expressions for the terms of the iteration series as Pe-dependent multiple integrals. We show that the series is convergent for $Pe \geqslant O(1)$, and that retaining only a few of its terms produces accurate results even for $Pe = O(1)$. An iterative procedure in the Fourier domain that leads to the same results is given by & Choi (2005).

4.1. *Zeroth-order solution via the Wiener–Hopf method*

The starting point of the analysis is the observation that, as discussed in §2.4, the solution for the semi-infinite strip $-1 < x < \infty$ (in the variable notation of (2.9)) provides the leading-order term of the high-Pe asymptotic expansion of the solution for the finite strip up to a distance $O(1/\sqrt{Pe})$ from the endpoint $x = 1$. In order to develop a systematical scheme for the correction terms, we symmetrize the kernel of (2.9) and rescale the independent variable x using $s = Pe(x + 1)$ while we define $\mu(s)$ by $\sigma(x) = (\sqrt{2}/\pi)\ Pe\, e^{s} \mu(s)$. (The factor $(\sqrt{2}/\pi)Pe$ is chosen for later convenience.) The integral equation (2.9) thus becomes

$$\int_0^{2Pe} ds' K_0(|s - s'|)\mu(s') = \frac{\pi^2 e^{-s}}{\sqrt{2}}, \quad 0 < s < 2Pe. \tag{4.1}$$

An approximate solution $\mu \sim \mu_0$ that is valid to the leading order in Pe is found by taking $Pe \to \infty$ in the upper limit of integration in (4.1). The resulting integral equation is

$$\int_0^{\infty} ds' K_0(|s - s'|)\mu_0(s') = \frac{\pi^2 e^{-s}}{\sqrt{2}}, \quad 0 < s. \tag{4.2}$$

The solution $\mu_0(s)$ is obtained by the Wiener–Hopf technique (Krein 1962; Noble 1988). Here we outline the basic steps of this method, which are also applied to other similar integral equations below. First, we extend the validity of (4.2) to $-\infty < s < \infty$ via modifying its right-hand side,

$$\int_{-\infty}^{\infty} ds' K_0(|s - s'|)\mu_0(s') = \frac{\pi^2}{\sqrt{2}}\{e^{-s} u(s) + p(s)\}, \quad -\infty < s < \infty, \tag{4.3}$$

where $\mu_0(s)$ is taken to be zero for $s < 0$, $u(s)$ is the Heaviside function ($u(s) = 0$ for $s < 0$ and $u(s) = 1$ for $s > 0$), and $p(s)$ is an unknown function which has non-zero values only for $s < 0$. Next, we apply the Fourier transform in s to (4.3). Defining the Fourier transform, $\tilde{\mu}_0(k)$, of $\mu_0(s)$ as

$$\tilde{\mu}_0(k) = \int_{-\infty}^{\infty} ds\, \mu_0(s)\, e^{-iks} \quad \text{where} \quad \mu_0(s) = \int_{-\infty}^{\infty} \frac{dk}{2\pi}\, e^{iks}\, \tilde{\mu}_0(k), \tag{4.4}$$

(4.3) yields

$$\frac{\pi\tilde{\mu}_0(k)}{\sqrt{1+k^2}} = \frac{\pi^2}{\sqrt{2}}\left[\frac{1}{1+\mathrm{i}k} + \tilde{p}(k)\right]. \tag{4.5}$$

By simple algebraic manipulations the last equation becomes

$$\frac{\tilde{\mu}_0(k)}{\sqrt{1+\mathrm{i}k}} - \frac{\pi}{1+\mathrm{i}k} = \frac{\pi}{\sqrt{2}}\left[\frac{\sqrt{1-\mathrm{i}k}-\sqrt{2}}{1+\mathrm{i}k} + \sqrt{1-\mathrm{i}k}\,\tilde{p}(k)\right], \tag{4.6}$$

where the left-hand side defines a function analytic in the lower half-k-plane, $\mathrm{Im}\,k < \varepsilon$ for a small positive ε, and the right-hand side defines a function analytic in the upper half-k-plane, $\mathrm{Im}\,k > -\varepsilon$; each of these functions vanishes as $|k| \to \infty$ in the corresponding half-plane. Thus, the two sides of (4.6) together define an entire function of k, which is identically zero by Liouville's theorem (Carrier *et al.* 1983). It follows that in the region of overlap, $|\mathrm{Im}\,k| < \varepsilon$, the solution is $\tilde{\mu}_0(k) = \pi(1+\mathrm{i}k)^{-1/2}$. Inversion of this formula yields

$$\mu_0(s) = \sqrt{\frac{\pi}{s}}\mathrm{e}^{-s}, \quad 0 < s < \infty. \tag{4.7}$$

4.2. *Leading-order uniformly accurate approximation*

The deviation of $\mu_0(s)$ in (4.7) from the actual solution $\mu(s)$ of the finite strip is interpreted as due to the effect of a fictitious 'misplaced' flux source lying in $2Pe < s$, which is present in (4.2). Therefore a correction term must be found for $\mu_0(s)$ by placing a 'correction source' on the original strip, $0 < s < 2Pe$, to compensate for the effect of the misplaced source. Margetis & Choi (2004) further develop this approach and place it on firm mathematical ground using Fourier transforms and a generalization of the Wiener–Hopf method. We proceed to calculate the correction to μ_0 iteratively. Accordingly, the solution $\mu(s)$ is sought in terms of the series

$$\mu = \mu_0 + \mu_1 + \mu_2 + \mu_3 + \cdots + \mu_n + \cdots, \tag{4.8}$$

where each term, $\mu_n(s)$, corresponds to suitable source corrections as described below.

We consider a half-line as the domain of the correction $\mu_1(s)$, as we did to obtain μ_0, but in the region $-\infty < s < 2Pe$ instead of the region $0 < s < \infty$. The term μ_1 is determined so that its effect compensates for the integrated effect of $\mu_0(s)$ in the region $2Pe < s$. Hence, the correction $\mu_1(s)$ satisfies

$$\int_{-\infty}^{2Pe} \mathrm{d}s' K_0(|s-s'|)\mu_1(s') = \int_{2Pe}^{\infty} \mathrm{d}s' K_0(|s-s'|)\mu_0(s'), \quad s < 2Pe, \tag{4.9}$$

where the right-hand side is known. The next-order corrections can be formulated and interpreted in a similar way; the correction μ_n compensates for the effect of the misplaced source corresponding to μ_{n-1}, where μ_{n-1} and μ_n are defined in half-lines that together cover the entire real axis and overlap only in the region of the finite strip. In general, $\mu_{n\geqslant 1}$ satisfy the recursion relations

$$\int_0^{\infty} K_0(|s-s'|)\mu_{n=2k}(s')\,\mathrm{d}s' = \int_{-\infty}^{0} K_0(|s-s'|)\mu_{n-1}(s')\,\mathrm{d}s', \tag{4.10a}$$

$$\int_0^{\infty} K_0(|v-v'|)\mu_{n=2k+1}(2Pe-v')\,\mathrm{d}v' = \int_{-\infty}^{0} K_0(|v-v'|)\mu_{n-1}(2Pe-v')\,\mathrm{d}v', \tag{4.10b}$$

where we made the change of variable from s to $v = 2Pe - s$ so that the integral equation for $\mu_{n=2k+1}$ has the same form as the one for $\mu_{n=2k}$. The variables s and v

are both positive ($s > 0$ and $v > 0$), the left endpoint ($x = -1$) of the strip corresponds to $s = 0$ and the right endpoint ($x = 1$) corresponds to $v = 0$.

The various μ_n can be obtained successively, order by order, by applying the Wiener–Hopf method (Krein 1962; Noble 1988) directly to (4.10), but the procedure becomes increasingly cumbersome with n. Instead, we propose a systematic procedure that facilitates the derivation of a closed-form expression for each μ_n. For this purpose, we introduce an operator, $\mathscr{L}$, that relates μ_{n-1} and μ_n by $\mathscr{L}[\mu_{n-1}] \equiv \mu_n$. By (4.10) $\mathscr{L}$ is linear. In order to obtain μ_1, we notice that the leading-order solution $\mu_0(s)$ can be represented as an integral over a variable, t_0,

$$\mu_0 = \sqrt{\frac{\pi}{s}}\mathrm{e}^{-s} = \int_{-\infty}^{\infty} \mathrm{d}t_0\, \mathrm{e}^{-s(1+t_0^2)}. \tag{4.11}$$

Then $\mathscr{L}$ acts on μ_0 to yield μ_1 as†

$$\mu_1 = \int \mathrm{d}t_0 \mathscr{L}\left[\mathrm{e}^{-s(1+t_0^2)}\right], \tag{4.12}$$

where the order of $\mathscr{L}$ and integration is safely interchanged. The advantage of using the t_0-representation is that $\mathrm{e}^{-s(1+t_0^2)}$, as a function of s, has a Fourier transform simpler than the Fourier transform of $\mu_0(s)$ itself. The function $\mathscr{L}[\mathrm{e}^{-s(1+t_0^2)}]$ is found by the Wiener–Hopf method (Krein 1962) as described in §4.2, and μ_1 follows by (4.12):

$$\mathscr{L}\left[\mathrm{e}^{-s(1+t_0^2)}\right] = \frac{\mathrm{e}^{-2Pe(1+t_0^2)}}{\pi\sqrt{2+t_0^2}}\left[\sqrt{\frac{\pi}{v}}\mathrm{e}^{-v} - \pi\sqrt{2+t_0^2}\,\mathrm{e}^{v(1+t_0^2)}\mathrm{erfc}\sqrt{v\left(2+t_0^2\right)}\right], \tag{4.13}$$

$$\mu_1(v) = K_0(2Pe)\frac{\mathrm{e}^{-v}}{\sqrt{\pi v}} - \int \mathrm{d}t_0\, \mathrm{e}^{-(2Pe-v)(1+t_0^2)}\mathrm{erfc}\sqrt{v\left(2+t_0^2\right)}. \tag{4.14}$$

Because μ_0 and μ_1 are accurate arbitrarily close to the left edge ($s = 0$) and the right edge ($v = 0$) of the strip, respectively, $\mu_0 + \mu_1$ yields a leading-order approximation for μ as $Pe \to \infty$ valid over the entire finite strip. The corresponding approximation for the flux $\sigma = (\sqrt{2}/\pi)Pe\,\mathrm{e}^{s}\mu(s)$ is $\sigma \sim \sigma_1 + \sigma_2$, which is given by

$$\sigma(x) \sim \sigma^{(\mathrm{hi})}(x) = 2\sqrt{\frac{Pe}{\pi}}\left\{\frac{1}{\sqrt{2(1+x)}} + \frac{K_0(2Pe)\mathrm{e}^{2Pe\,x}}{\pi\sqrt{2(1-x)}} - \int \mathrm{d}t\,\tau\frac{\mathrm{e}^{-(1+x)\tau^2}}{\sqrt{2\pi}}\mathrm{erfc}\sqrt{(2Pe+\tau^2)(1-x)}\right\} \tag{4.15}$$

for the geometry of the finite strip, and

$$\sigma(\theta) \sim \sigma^{(\mathrm{hi})}(\theta) = 2\sqrt{\frac{Pe}{\pi}}\left\{\left|\sin\frac{\theta}{2}\right| + \frac{1}{\pi}K_0(2Pe)\mathrm{e}^{2Pe\cos\theta}\left|\cos\frac{\theta}{2}\right| - \frac{|\sin\theta|}{\sqrt{2\pi}}\int \mathrm{d}t\,\tau\,\mathrm{e}^{-(1+\cos\theta)\tau^2}\mathrm{erfc}\sqrt{(2Pe+\tau^2)(1-\cos\theta)}\right\} \tag{4.16}$$

for the geometry of the unit circular disk. In the last formula we changed the variable to $\tau = \sqrt{Pe}\ t_0$. An expansion similar to (4.15) has been obtained by Chugunov & Kornev (1986) and Kornev & Chugunov (1988) in the physical context of artificial

† In the remaining integrals of this section the range of integration is understood to be from $-\infty$ to ∞ unless it is stated otherwise.

freezing but we could not verify whether (4.15) is equivalent to (13) in Chugunov & Kornev (1986) or (3.7) in Kornev & Chugunov (1988); these authors did not use the operator $\mathscr{L}$ in their method and apparently did not obtain higher-order terms. An elaborate mathematical procedure for asymptotic solutions to the relevant class of integral equations on the basis of kernel approximations is described in Aleksandrov & Belokon (1968) and Aleksandrov & Pozharskii (1999). We note that $\sigma_0(x)$ and $\sigma_1(x)$ are singular at $x=-1$ and $x=1$, respectively, the edges of the finite strip; these singularities are properly removed after the strip is mapped onto the unit disk.

4.3. *Exact higher-order terms*

In an effort to obtain further insight into the nature of the solution σ of (2.9), we next derive exact closed-form expressions for μ_n for all n in terms of iterated multiple integrals. For this purpose, we exploit the $\mathscr{L}$ operator introduced above. We observe that (4.13) has the integral representation

$$\mathscr{L}\left[\mathrm{e}^{-s(1+t_0^2)}\right] = \int \mathrm{d}t_1 \frac{\mathrm{e}^{-2Pe(1+t_0^2)}}{\pi\sqrt{2+t_0^2}} \frac{t_1^2}{2+t_0^2+t_1^2} \mathrm{e}^{-v(1+t_1^2)}, \tag{4.17}$$

where the last factor in the integrand has the same form as the $\mathrm{e}^{-s(1+t_0^2)}$ term, on which the $\mathscr{L}$ acts in (4.12), with s being replaced by v and t_0 being replaced by t_1. It follows that the μ_n is expressed as the nth power of $\mathscr{L}$ acting on a term of the form $\mathrm{e}^{-s(1+t^2)}$, $\mathscr{L}^n[\mathrm{e}^{-s(1+t^2)}]$. Thus, by induction, μ_n is expressed as an iterated multiple integral of the independent variable s or v,

$$\mu_n(u) = \mathrm{e}^{-2nPe} \int \mathrm{d}t_0 \int \mathrm{d}t_1 (Q_0 R_1) \int \mathrm{d}t_2 (Q_1 R_2) \cdots \int \mathrm{d}t_n (Q_{n-1} R_n) \mathrm{e}^{-u(1+t_n^2)}, \tag{4.18}$$

where $u \equiv s$ for even n and $u \equiv v$ for odd n, and Q_n and R_n are defined by

$$Q_n \equiv \frac{\mathrm{e}^{-2Pe\, t_n^2}}{\pi\sqrt{2+t_n^2}}, \qquad R_n \equiv \frac{t_n^2}{2+t_{n-1}^2+t_n^2}. \tag{4.19}$$

As indicated from (4.13), $\mu_n(u)$ has has the singularity $u^{-1/2}$ at $u=0$ which comes from the last integral of (4.18). Thus we can single out the singular behaviour as $\mu_n(u) = \sqrt{\pi/u}\, \mathrm{e}^{-2nPe-u}\, F_n(u)$ and the singular-free part, F_n, is given by

$$F_n(u) = \int \mathrm{d}t_0 \int \mathrm{d}t_1 (Q_0 R_1) \int \mathrm{d}t_2 (Q_1 R_2) \cdots$$
$$\cdots \int \mathrm{d}t_{n-1} (Q_{n-2} R_{n-1}) \left[Q_{n-1} - \sqrt{\frac{u}{\pi}}\, \mathrm{e}^{2u-(2Pe-u)t_{n-1}^2} \mathrm{erfc}\sqrt{u\left(2+t_{n-1}^2\right)} \right], \tag{4.20}$$

where (4.13) and (4.17) are used to evaluate the last integral.

Thus, the nth term for the flux on the strip, $\sigma_n(x)$, is given by

$$\sigma_{n=2k}(x) = 2\sqrt{\frac{Pe}{\pi}} \frac{\mathrm{e}^{-2nPe}}{\sqrt{2(1+x)}} F_n(Pe(1+x)), \tag{4.21a}$$

$$\sigma_{n=2k+1}(x) = 2\sqrt{\frac{Pe}{\pi}} \frac{\mathrm{e}^{-2(n-x)Pe}}{\sqrt{2(1+x)}} F_n(Pe(1-x)). \tag{4.21b}$$

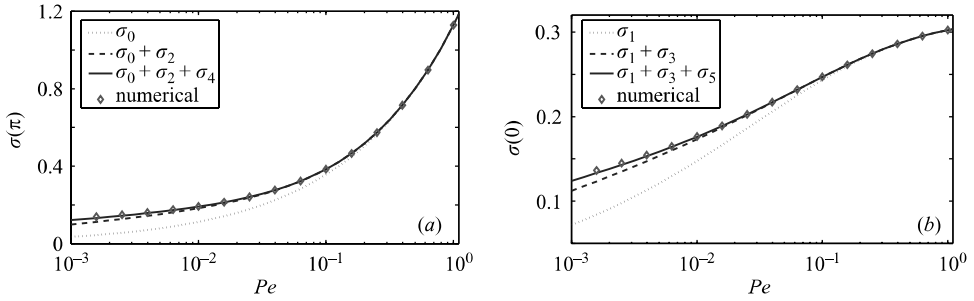

FIGURE 7. Asymptotic approximations for high Pe compared with our numerical solution: (*a*) upstream flux, $\sigma(\theta=\pi;Pe)$ and (*b*) downstream flux, $\sigma(\theta=0;Pe)$. The integrals in the asymptotic corrections, σ_n $(1\leqslant n\leqslant 5)$, were performed numerically.

On the unit circle $\sigma_n(\theta)$ is free of singularities in θ and is expressed as

$$\sigma_{n=2k}(\theta)=2\sqrt{\frac{Pe}{\pi}}\mathrm{e}^{-2nPe}\left|\sin\frac{\theta}{2}\right|F_n(Pe(1+\cos\theta)), \tag{4.22a}$$

$$\sigma_{n=2k+1}(\theta)=2\sqrt{\frac{Pe}{\pi}}\mathrm{e}^{-2(n-\cos\theta)Pe}\left|\cos\frac{\theta}{2}\right|F_n(Pe(1-\cos\theta)). \tag{4.22b}$$

It has not been possible to evaluate σ_n from (4.22) in simple closed form, except for $n=1,\ 2$, as described by (4.16). However, the numerical integrations over the variables t_j $(j=1,2,\ldots n)$ for each σ_n can be carried out efficiently by using recursion.

We verify that the sum for the flux, $\sigma\sim\sigma_0+\sigma_1+\cdots+\sigma_n$, calculated for finite n via the numerical integration of (4.22), indeed approaches the numerical solution of § 3. In figure 7, we show a comparison of the numerical solution of § 3 for $\sigma(0)$ and $\sigma(\pi)$ with formula (4.22) for different values of n. Because $\sigma_{n=2k}(\theta)$ and $\sigma_{n=2k+1}(\theta)$ vanish at $\theta=0$ and $\theta=\pi$, respectively, the term $\sigma_{n=2k}(\theta)$ affects only $\sigma(\pi)$ whereas the term $\sigma_{n=2k+1}(\theta)$ affects only $\sigma(0)$.

Remarkably, with only a few terms, our approximation is uniformly accurate down to values of Pe of order 10^{-2} or lower, which could hardly be called 'high', while some correction terms $\mu_{n\geqslant 2}$ may not be small. This behaviour suggests that there may be an intermediate region of overlap between asymptotic approximations for high and low Pe. Indeed, by combining such approximations below, we will construct a very accurate approximation for all θ and all Pe.

The closed-form expression of σ_n also serves as another 'numerical method' for high Pe. The multiple integrals in (4.20) can be numerically evaluated in a recursive way; the intermediate calculation steps for F_k recur in the calculation for all $F_{n>k}$. Thus, the computational cost for $\sum_{k=0}^{n}\sigma_k$ is the same as that for σ_n, which scales linearly with n.

4.4. *Convergence of the asymptotic series*

We next discuss the convergence properties of the asymptotic series $\sum_n\sigma_n(\theta)$ for σ on the unit circle. Because the maximum of $\sigma_n(\theta)$ occurs at $\theta=\pi$ for $n=2k$ and at $\theta=0$ for $n=2k+1$, it is readily shown that

$$\|\sigma_0\|=2\sqrt{\frac{Pe}{\pi}}\quad\text{and}\quad\begin{cases}\|\sigma_{n=2k}\|=\mathrm{e}^{-4Pe\,k}\|F_{2k}\|\,\|\sigma_0\|\\ \|\sigma_{n=2k+1}\|=\mathrm{e}^{-4Pe\,k}\|F_{2k+1}\|\,\|\sigma_0\|,\end{cases} \tag{4.23}$$

From (4.20), $\|F_n\|$ is simply $F_n(u=0)$. In particular, for $n=1, 2$, $\|F_n\|$ are evaluated in simpler forms:

$$\|F_1\| = \frac{\mathrm{e}^{2Pe}}{\pi} K_0(2Pe), \quad \|F_2\| = \frac{\mathrm{e}^{4Pe}}{\pi^2}\left\{\frac{K_0(2Pe)^2}{2} - \int_{2Pe}^{\infty} \mathrm{d}t\, K_0(t)^2\right\}. \tag{4.24}$$

We have not been able to further simplify the expressions for $\|F_{n>2}\|$. We now show that each $\|F_n\|$ is bounded by a function of Pe that ensures convergence of the series $\sum_n \sigma_n$ for $Pe \geqslant O(1)$. By noting that $Q_n < \mathrm{e}^{-2Pe\, t_n^2}/\sqrt{2}$ and $R_n < 1/\pi$, we find

$$\|F_n\| < \pi^{-n/2}\,(4Pe)^{-n/2}, \tag{4.25}$$

for any $Pe > 0$. Hence, by (4.23) the series $\sum_n \sigma_n$ is characterized by geometric convergence in the parameter $Pe^{-1/2}$ for $Pe \geqslant O(1)$. Finally, for large Pe and fixed n the asymptotic behaviour of $\|F_n\|$ with respect to Pe is obtained via scaling the original variables t_k as $\tau_k = t_k\sqrt{2Pe}$ $(k=0,\ldots,n-1)$,

$$\|F_{n\geqslant 1}\| \sim \frac{1}{2\sqrt{\pi Pe}}\left(\frac{1}{16\sqrt{\pi}Pe^{3/2}}\right)^{n-1} \quad \text{as } Pe \to \infty. \tag{4.26}$$

Formulae (4.25) and (4.26) indicate that the series $\sum_n \sigma_n$ converges geometrically for a wide range of Pe.

We check numerically that $\|F_n\|$ decays exponentially in n for a wide range of Pe, $\|F_n\| \sim \rho^{-n}$ as $n \to \infty$ where $\rho = \rho(Pe) > 0$ is the 'decay rate' of $\|F_n\|$, which is independent of n. For this purpose, we examine the ratio $\|F_n\|/\|F_{n+1}\|$ as a function of both n and Pe, expecting that this ratio approaches a constant for fixed Pe as n becomes sufficiently large, as shown in figure 8(*a–c*). From figure 8(*d*) we find that the relative error in the approximation of σ by the sum $\sum_{k=1}^{5} \sigma_k$ becomes higher than 1% only when $Pe < 6.5 \times 10^{-3}$.

5. Uniformly accurate asymptotics for low Péclet numbers

In this section we solve approximately the integral equation (2.9) for the surface flux $\sigma(x)$, for all x in $(-1, 1)$, when Pe is sufficiently small, $Pe < O(1)$. For this purpose, we define the dependent variable $\varphi(x) = \mathrm{e}^{-Pe\,x}\sigma(x)$. Equation (2.9) thus becomes

$$\int_{-1}^{1} \mathrm{d}x'\, K_0(Pe|x-x'|)\varphi(x') = \pi \mathrm{e}^{-Pe\,x}, \qquad -1 < x < 1. \tag{5.1}$$

Because the argument of the kernel is also sufficiently small, $Pe|x-x'| < O(1)$, we invoke the expansion

$$K_0(Pe|x-x'|) \sim -I_0(Pe|x-x'|)\ln\left(\frac{Pe}{2}|x-x'|\right) + \sum_{m=0}^{M} \frac{\psi(m+1)}{(m!)^2}\left(\frac{Pe|x-x'|}{2}\right)^{2m}, \tag{5.2}$$

where it is understood that

$$I_0(Pe|x-x'|) \sim \sum_{m=0}^{M} \frac{2^{-2m}Pe^{2m}|x-x'|^{2m}}{(m!)^2}, \tag{5.3}$$

and $\psi(z)$ is the logarithmic derivative of the Gamma function, $\psi(z) = \mathrm{d}/\mathrm{d}z \ln\Gamma(z)$. It was first pointed out by Pearson (1957) that the resulting integral equation can be solved exactly for any finite number of terms, M, but the procedure becomes increasingly cumbersome with M.

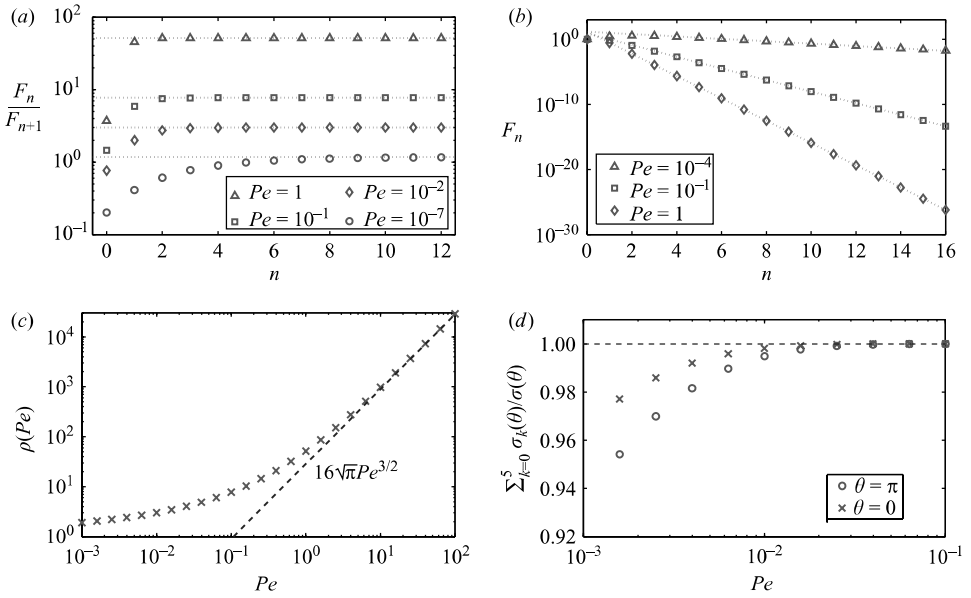

FIGURE 8. Numerical evidence for the convergence of the iteration series $\sum_n \sigma_n \sim \sigma$. (*a*) The ratio $\|F_n\|/\|F_{n+1}\|$ as a function of n for different values of Pe. The convergence of $\sum_n \sigma_n$ is guaranteed if $\|F_n\|/\|F_{n+1}\| > 1$ by virtue of (4.23). (*b*) The term $\|F_n\|$ as a function of n for different values of Pe. (*c*) The decay rate $\rho(Pe)$ of $\|F_n\|$ as a function of Pe, where $\rho = \lim_{n\to\infty}(\|F_n\|/\|F_{n+1}\|)$. The asymptotic behaviour (4.26) is shown to be attained for $Pe > 10$. (*d*) The ratio of $\sum_{k=1}^{5}\sigma_k(\theta)$ to $\sigma(\theta)$ as a function of small values of Pe and $\theta = 0$, π, where $\sigma(\theta)$ is evaluated numerically by the method of § 3.

To leading order we consider $M = 0$ in (5.2) and (5.3). Equation (5.1) thus reduces to a variant of Carleman's equation (Carleman 1922),

$$\int_{-1}^{1} \mathrm{d}x' \ln(|x - x'|)\varphi_0(x') = C_1 - \pi \mathrm{e}^{-Pe\,x}, \tag{5.4}$$

where $\varphi_0(x) \sim \varphi(x)$ is the corresponding approximation for $\varphi(x)$ and C_1 is the constant

$$C_1 = -[\gamma + \ln(Pe/2)] \int_{-1}^{1} \mathrm{d}x'\varphi_0(x'), \tag{5.5}$$

where $\gamma = -\psi(1) = 0.577215\cdots$ is the Euler number.
Following Carrier *et al.* (1983), we introduce the complex function

$$\Phi(z) = \frac{\sqrt{z^2 - 1}}{2\pi \mathrm{i}} \int_{-1}^{1} \mathrm{d}x' \, \frac{\varphi_0(x')}{x' - z} \tag{5.6}$$

and single out the limit values

$$\Phi^{\pm}(x) \equiv \lim_{\varepsilon\to 0} \Phi(x \pm \mathrm{i}\varepsilon) = \pm \frac{\sqrt{1 - x^2}}{2\pi} \lim_{\varepsilon\to 0} \int_{-1\mp\mathrm{i}\varepsilon}^{1\mp\mathrm{i}\varepsilon} \mathrm{d}z' \, \frac{\varphi_0(z')}{z' - x}, \tag{5.7}$$

by which the integral equation (5.4) is equivalent to the equations

$$\Phi^+(x) - \Phi^-(x) = -\frac{\sqrt{1-x^2}}{\pi}\frac{\mathrm{d}}{\mathrm{d}x}\int_{-1}^{1}\mathrm{d}x'\,\ln(|x-x'|)\,\varphi_0(x') = -Pe\sqrt{1-x^2}\,\mathrm{e}^{-Pe\,x}, \quad (5.8)$$

$$\Phi^+(x) + \Phi^-(x) = \mathrm{i}\sqrt{1-x^2}\,\mathrm{Res}\left\{\frac{\varphi_0(z')}{z'-x}; z'=x\right\} = \mathrm{i}\sqrt{1-x^2}\,\varphi_0(x). \quad (5.9)$$

First, we find $\Phi(z)$ via applying directly the Mittag–Leffler expansion theorem to (5.8) (Carrier *et al.* 1983):

$$\Phi(z) = -\frac{1}{2\pi\mathrm{i}}\left(Pe\int_{-1}^{1}\mathrm{d}x'\,\frac{\sqrt{1-x'^2}}{x'-z}\,\mathrm{e}^{-Pe\,x'} + A\right), \quad (5.10)$$

where $-(2\pi\mathrm{i})^{-1}A$ is the limit as $z\to\infty$ of the function $\Phi(z)$; by inspection of (5.6),

$$A = \int_{-1}^{1}\mathrm{d}x'\,\varphi_0(x'). \quad (5.11)$$

We recognize that the constant C_1 of (5.5) is $C_1 = -[\gamma + \ln(Pe/2)]A$.

Next, we obtain the approximate solution $\varphi_0(x)$ in terms of this A by (5.8):

$$\varphi_0(x) = \frac{1}{\pi\sqrt{1-x^2}}\left[Pe\,(P)\int_{-1}^{1}\mathrm{d}x'\,\frac{\sqrt{1-x'^2}}{x'-x}\,\mathrm{e}^{-Pe\,x'} + A\right], \quad (5.12)$$

where $(P)\int_{-1}^{1}$ denotes the principal value of the integral. In order to determine the unknown constant A, we multiply both sides of (5.4) by $(1-x^2)^{-1/2}$ and integrate over $(-1, 1)$ by use of the elementary integral (Carrier *et al.* 1983)

$$\int_{-1}^{1}\mathrm{d}x\,\frac{\ln(|x-x'|)}{\sqrt{1-x^2}} = -\pi\ln 2. \quad (5.13)$$

A few comments on this result are in order. It can be obtained via differentiating the left-hand side with respect to x', and thus converting the integral to a Cauchy principal value which is found directly to vanish identically. Hence, the original integral is independent of x' and can be evaluated for $x'=0$ by changing the variable to $x = (\xi - 1/\xi)/(2\mathrm{i})$, where ξ moves on the unit circle, and applying the residue theorem (Carrier *et al.* 1983). We thus find

$$A = -\frac{1}{\gamma + \ln(Pe/4)}\int_{-1}^{1}\mathrm{d}x\,\frac{\mathrm{e}^{-Pe\,x}}{\sqrt{1-x^2}}, \quad (5.14)$$

$$\varphi_0(x) = \frac{1}{\pi\sqrt{1-x^2}}\left[Pe\,(P)\int_{-1}^{1}\mathrm{d}x'\,\frac{\sqrt{1-x'^2}}{x'-x}\,\mathrm{e}^{-Pe\,x'} - \frac{1}{\gamma+\ln(Pe/4)}\int_{-1}^{1}\mathrm{d}x'\,\frac{e^{-Pe\,x'}}{\sqrt{1-x'^2}}\right]. \quad (5.15)$$

It is straightforward to carry out the integrations in (5.15). The second integral on the right-hand side is simply a modified Bessel function of the first kind:

$$\int_{-1}^{1}\mathrm{d}x\,\frac{\mathrm{e}^{-Pe\,x}}{\sqrt{1-x^2}} = \int_{0}^{\pi}\mathrm{d}t\,\mathrm{e}^{-Pe\cos t} = \pi J_0(\mathrm{i}Pe) = \pi I_0(Pe). \quad (5.16)$$

The remaining integral can be converted to one that is directly amenable to numerical computation for $Pe \leqslant O(1)$. By defining

$$\mathscr{I}(Pe; x) = (P)\int_{-1}^{1}\mathrm{d}x'\,\frac{\sqrt{1-x'^2}}{x'-x}\,\mathrm{e}^{-Pe(x'-x)}, \quad (5.17)$$

we evaluate the derivative

$$\mathrm{e}^{-Pe\,x}\frac{\partial \mathscr{I}}{\partial Pe} = -\int_{-1}^{1} \mathrm{d}x'\,\sqrt{1-x'^2}\,\mathrm{e}^{-Pe\,x'} = -\pi[I_0(Pe) - I_0''(Pe)] = -\pi\,\frac{I_1(Pe)}{Pe}, \tag{5.18}$$

where I_ν is the modified Bessel function of the first kind. An expression for the integral (5.17) then follows by direct integration in Pe of (5.18):

$$\mathscr{I}(Pe;x) = \mathscr{I}(0;x) - \pi\int_0^{Pe} \mathrm{d}t\ \mathrm{e}^{tx}\,\frac{I_1(t)}{t}, \tag{5.19}$$

where

$$\mathscr{I}(0;x) = -(1-x^2)\,\frac{\mathrm{d}}{\mathrm{d}x}\int_{-1}^{1}\mathrm{d}x'\ \frac{\ln(|x-x'|)}{\sqrt{1-x'^2}} - \pi x = -\pi x. \tag{5.20}$$

Hence,

$$\mathscr{I}(Pe;x) = -\pi x - \pi\int_0^{Pe} \mathrm{d}t\ \mathrm{e}^{tx}\,\frac{I_1(t)}{t}. \tag{5.21}$$

The approximation

$$\gamma + \ln(Pe/4) \sim -K_0(Pe/2), \tag{5.22}$$

which becomes useful in § 6 where we construct a uniform formula for all Pe and local coordinate of the boundary, and the use of (5.16), (5.21) and $\sigma(x) = \mathrm{e}^{Pe\,x}\varphi(x)$ yield a low-Pe approximation for the flux on the boundary of the finite strip, $\sigma^{(\mathrm{lo})} = \mathrm{e}^{Pe\,x}\varphi_0(x)$,

$$\sigma(x) \sim \sigma^{(\mathrm{lo})}(x) = \frac{1}{\sqrt{1-x^2}}\left\{\frac{I_0(Pe)}{K_0(Pe/2)}\,\mathrm{e}^{Pe\,x} - Pe\left[x + \int_0^{Pe}\mathrm{d}t\ \mathrm{e}^{tx}\,\frac{I_1(t)}{t}\right]\right\}. \tag{5.23}$$

Hence, by virtue of (2.15), the flux on the unit circle is

$$\sigma(\theta) \sim \sigma^{(\mathrm{lo})}(\theta) = \frac{I_0(Pe)}{K_0(Pe/2)}\,\mathrm{e}^{Pe\cos\theta} - Pe\left[\cos\theta + \int_0^{Pe}\mathrm{d}t\ \mathrm{e}^{t\cos\theta}\,\frac{I_1(t)}{t}\right]. \tag{5.24}$$

We note in passing that the integral in (5.23) can be expressed as a power series in Pe. With the series expansions

$$\mathrm{e}^{tx} = \sum_{n=0}^{\infty}\frac{t^n x^n}{n!}, \qquad \frac{I_1(t)}{t} = \sum_{m=0}^{\infty}\frac{t^{2m}}{2^{2m+1}}\,\frac{1}{m!\,(m+1)!}, \tag{5.25}$$

it is straightforward to derive the expansion

$$\begin{aligned}\int_0^{Pe}\mathrm{d}t\ \mathrm{e}^{xt}\,\frac{I_1(t)}{t} = &\sum_{l=0}^{\infty}\frac{Pe^{2l+1}}{2l+1}\sum_{m=0}^{l}\frac{x^{2m}}{(2m)!\,(l-m)!\,(l-m+1)!}\\ &+\sum_{l=0}^{\infty}\frac{Pe^{2(l+1)}}{2(l+1)}\sum_{m=0}^{l}\frac{x^{2m+1}}{(2m+1)!\,(l-m)!\,(l-m+1)!}.\end{aligned} \tag{5.26}$$

A few comments on formula (5.23) are in order. Aleksandrov & Belokon (1967) expanded to high orders the kernels of the relevant class of singular integral equations and derived in generality a more accurate yet complicated formula for the solution. The procedure here, though being based on simply taking $M = 0$ in (5.2) and (5.3), leaves intact the right-hand side of (5.1) and applies (5.22); our approximate formula for $\sigma(x)$ turns out to be accurate for an extended range of low Pe. Figure 9 shows a comparison of (5.24) with the numerical solution of § 3 for a range of low Péclet numbers.

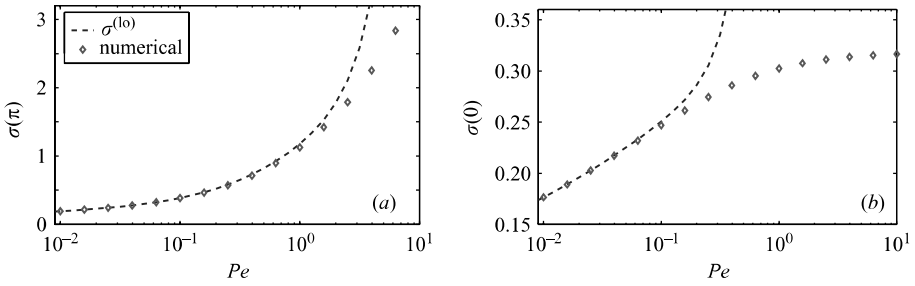

FIGURE 9. The asymptotic approximation $\sigma^{(lo)}(\theta; Pe)$ in (5.24) compared to the numerical solution of § 3 for a range of low Pe. (*a*) Upstream flux, $\sigma^{(lo)}(\theta = \pi; Pe)$, and (*b*) downstream flux, $\sigma^{(lo)}(\theta = 0; Pe)$.

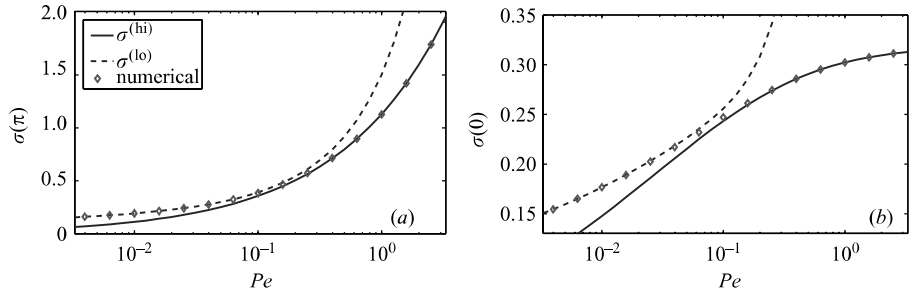

FIGURE 10. Plots of formulae (4.16) for $\sigma^{(hi)}$ and (5.24) for $\sigma^{(lo)}$ versus Pe in the same graph as the plot for the solution σ evaluated numerically by the method of § 3. (*a*) Upstream flux, $\sigma(\theta = 0; Pe)$, (*b*) downstream flux, $\sigma(\theta = \pi; Pe)$.

6. Uniformly accurate formula for all positions and Péclet numbers

6.1. *Connecting the high and low Pe approximations for the flux*

In §§ 4 and 5 we derived asymptotic formulae for the surface flux σ on the boundary of the unit circular disk (or finite strip) that are valid for sufficiently high or sufficiently low Pe; these expressions, $\sigma^{(hi)}$ and $\sigma^{(lo)}$ in (4.16) and (5.24), respectively, hold for all values of the local coordinate of the absorber boundary, although we did not analyse to what extent the approximations are uniformly valid in a rigorous mathematical sense. Comparisons with the numerical results in figures 7 and 9 show that the approximations are comparably accurate for the rear stagnation point ($\theta = 0$) and forward stagnation point ($\theta = \pi$). We have also checked that, for fixed Pe, the errors are also comparable at intermediate values of the local coordinate ($0 < \theta < \pi$). In figure 10, we show that the two approximations, $\sigma^{(hi)}$ and $\sigma^{(lo)}$, nearly overlap for some range of values Pe near $Pe = 0.1$, while remaining remarkably close to the 'exact' numerical solution from § 3.

The existence of a regime of overlapping accuracy allows us to construct an analytical formula for σ, accurate for all values of Pe and the local coordinate of the absorbing boundary, θ, by smoothly connecting $\sigma^{(hi)}$ and $\sigma^{(lo)}$. A similar overlapping accuracy was found for a three-dimensional problem of heat or mass transfer in a steady shear flow by Phillips (1990), who combined high- and low-Pe expansions only for the Nusselt number, Nu, using singular perturbation. The dependence of the flux

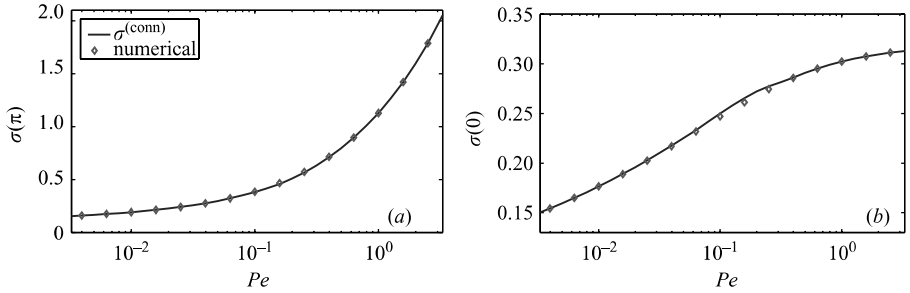

FIGURE 11. Plots of the connection formula, $\sigma^{(\mathrm{conn})}$, from § (6.1) and (6.3), in comparison to the numerical solution of § 3 (*a*) Upstream flux, $\sigma(\theta = \pi; Pe)$, and (*b*) downstream flux, $\sigma(\theta = \pi; Pe)$. The relative error of $\sigma^{(\mathrm{conn})}$ compared to the numerical solution is less than 1.75% for all values of Pe and θ, and it becomes negligibly small at high and low Pe for all θ.

σ on Pe can be described heuristically by a formula of the form

$$\sigma(\theta; Pe) \sim \sigma^{(\mathrm{conn})} = \sigma^{(\mathrm{hi})}(\theta; Pe)\,\mathscr{U}(Pe/P_o) + \sigma^{(\mathrm{lo})}(\theta; Pe)\,[1 - \mathscr{U}(Pe/P_o)], \tag{6.1}$$

for the entire range of Pe and θ; $\mathscr{U}(\chi)$ is a family of smooth functions defined for $\chi = Pe/P_0 > 0$ that at least satisfy the conditions

$$\lim_{\chi \to 0^+} \mathscr{U}(\chi) = 0, \qquad \lim_{\chi \to +\infty} \mathscr{U}(\chi) = 1. \tag{6.2}$$

A simple choice for the step-like function, $\mathscr{U}$, which yields a rather accurate formula for σ, is

$$\mathscr{U}(\chi; \alpha) = \mathrm{e}^{1/(1-\exp \chi^{\alpha})}, \qquad \alpha > 0. \tag{6.3}$$

We note that there are two free parameters in (6.3) with $\chi = Pe/P_0$: α and P_0. The parameter P_0 corresponds to a value of P_0 in the region of overlap of formulae (4.16) and (5.24); in principle, P_0 may depend on the local coordinate, which is θ for the unit circle. The parameter α determines the steepness of the curve $\mathscr{U}(\chi)$ near $\chi = 1$.

We find that a good fit with the numerical solution is achieved for $\alpha = 2$ and $P_0 = 1/6$, as shown in figure 11 where $\sigma^{(\mathrm{conn})}(\theta)$ is plotted versus Pe for $\theta = \pi$ (upstream flux) and $\theta = 0$ (downstream flux). The relative error is less than 1.75% for all values of Pe and θ. Because we have the exact Green's function (2.7), this uniform accuracy also carries over to the solution of the entire concentration field, $c(x, y; Pe)$, obtained from the integral (2.8).

Our analytical approximation also describes an absorber of arbitrary shape obtained by conformal mapping, $z = g(w)$ $(w = \mathrm{e}^{\mathrm{i}\theta})$. The flux distribution on the unit circle, $\sigma^{(\mathrm{conn})}(\theta)$, is transformed to the new surface using (2.14). Because the flux is proportional to a gradient, it is locally amplified by a factor of $|g'(w)|^{-1}$, which may cause relative errors larger than 1.75% in some locations, e.g. near a cusp, where conformality breaks down ($g' = 0$). For a well-behaved univalent mapping, however, the approximation should remain very accurate for all positions, $g(\mathrm{e}^{\mathrm{i}\theta})$ and Pe, so the general BVP may be considered effectively solved.

6.2. *The total flux to the absorber*

It is straightforward to obtain a uniformly accurate approximation of the Nusselt number by integrating the flux on the unit circle or the finite strip:

$$Nu(Pe) = \int_0^{2\pi} \mathrm{d}\theta\, \sigma(\theta; Pe) = 2 \int_{-1}^{1} \mathrm{d}x\, \sigma(x; Pe). \tag{6.4}$$

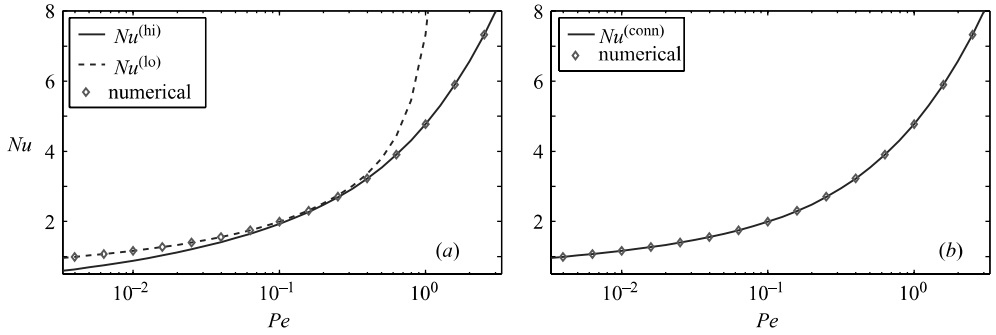

FIGURE 12. The Nusselt number, Nu, which gives the total flux to the absorber, versus the Péclet number, quantifying the importance of advection compared to diffusion. In (*a*) the asymptotic expressions (6.5) overlap for $0.1 < Pe < 0.4$. In (*b*) the analytical connection formula (6.6) compares very well with the 'exact' numerical result from § 3. The results hold for absorbers of arbitrary shape, as long as Pe is the renormalized Péclet number, $Pe = A_1\, Pe_o$, where A_1 is the conformal radius and Pe_o is the bare Péclet number for the unit circle.

The leading-order expressions for $Nu(Pe)$ in the high- and low-Pe limits are thus obtained by integrating (4.15) and (5.23) using integration by parts and the identity $x I_0(x) = [x I_1(x)]'$ (Gradshteyn & Ryzhik 1980),

$$Nu^{(\mathrm{hi})}(Pe) = \frac{8}{\pi}\left\{\sqrt{\frac{Pe}{\pi}}\,\mathrm{e}^{-2Pe}K_0(2Pe) + Pe\,\mathrm{e}^{2Pe}\mathrm{erf}(2\sqrt{Pe})[K_0(2Pe) + K_1(2Pe)]\right\}, \quad (6.5a)$$

$$Nu^{(\mathrm{lo})}(Pe) = 2\pi\left\{\frac{I_0(Pe)^2}{K_0(Pe/2)} + (Pe)^2[I_1(Pe)^2 - I_0(Pe)^2] + Pe I_0(Pe)\, I_1(Pe)\right\}. \quad (6.5b)$$

The uniform analytical approximation for $Nu(Pe)$ follows as

$$Nu^{(\mathrm{conn})}(Pe) = Nu^{(\mathrm{hi})}(Pe)\,\mathrm{e}^{1/(1-\exp(36Pe)^2)} + Nu^{(\mathrm{lo})}(Pe)\left[1 - \mathrm{e}^{1/(1-\exp^{36Pe^2})}\right]. \quad (6.6)$$

As shown in figure 12, this analytical result is quite accurate over the entire range of Péclet numbers, and it becomes exact as $Pe \to 0$ and $Pe \to \infty$. The maximum relative error is found to be 0.53 %. We are not aware of any such analytical formula for the complete Nusselt–Péclet relation of a finite absorber.

It may come as a surprise that the same result (6.5) also holds for an absorber of arbitrary shape, obtained by conformal mapping of the unit circle, $z = g(w)$, without any additional error. The reason is that the total flux through any contour is preserved *exactly* under every conformal mapping of a conformally invariant BVP (Bazant 2004). When computing Nu from (6.4) for another shape, therefore, one must simply use the renormalized Péclet number, $Pe = A_1 Pe_o$, equal to the conformal radius, A_1, times the bare Péclet number, Pe_o, for the unit circle.

7. Conclusion

7.1. *Summary of results*

We have performed a detailed study of the BVP (1.3)–(1.5) for a finite absorber of arbitrary cross-section in a steady two-dimensional potential flow. Our focus has been the flux profile on the boundary, σ, from which the concentration can be obtain everywhere in the plane by convolution with the known Green's function. We have explicitly considered several simple cases, notably the canonical problem of

uniform flow past a circular cylinder, which can be mapped to arbitrary geometries by conformal mapping, as described in § 2.

In § 3, we presented an efficient numerical method to solve the BVP. We began by mapping the BVP to the inside of the unit circle in order to work with a bounded domain. We then eliminated some 'far-field' singularities (at the origin) using exact asymptotics and applied a spectral method in polar coordinates, with exponential convergence in the number of nodes. We also used an adaptive mesh to deal with boundary layers at very high Péclet numbers. The results, which are illustrated in figures 2 and 4, provided reliable tests of our analytical approximations.

In §§ 4 and 5, we derived distinct asymptotic expansions for the flux on the boundary of the finite strip for high and low *Pe*, respectively, starting from a well-known integral equation in streamline coordinates (Van Wijngaarden 1966), which has been studied extensively in the theory of solidification and freezing in a flowing melt (Maksimov 1976; Chugunov & Kornev 1986; Kornev & Chugunov 1988; Kornev & Mukhamadullina 1994; Alimov *et al.* 1994, 1998; Cummings & Kornev 1999; Cummings *et al.* 1999). We used some original variations on classical techniques from the theory of singular integral equations, including the Wiener–Hopf method of factorization, to obtain improvements on previous approximations.

Noteworthy features of our expansions for high *Pe* are: (i) the summands admit closed-form expressions in terms of multiple integrals (4.22), which are straightforward to evaluate numerically; (ii) the expansions converge for all distances along the strip for a wide range of *Pe*, $Pe \geqslant O(10^{-2})$; and (iii) only the small number of terms in (4.16) need be retained for reasonable accuracy though the number increases as *Pe* decreases. On the other hand, our asymptotic formula (5.24) for low *Pe* is accurate for $Pe \leqslant 10^{-1}$, which renders it possible to have a region where the two expansions overlap.

Therefore, we were able to construct an *ad hoc* analytical connection formula (6.1), which reproduces our numerical results for the flux to a circular absorber with less than 1.75% relative error for all angles and Péclet numbers, as shown in figure 11. We also predicted the *Nu*(*Pe*) relation (6.4) with comparable accuracy, as shown in figure 12. These results constitute a nearly exact analytical solution to the BVP (1.3)–(1.5).

The main contribution of our work is a unified description of the crossover regime, intepolating between the well-known asymptotic limits of high and low *Pe*. As such, we can draw some mathematical and physical conclusions about the transition in the following sections.

7.2. *Mathematical discussion*

A posteriori, we may try to understand why perturbation methods, which ostensibly require extreme values of *Pe*, produce a very accurate analytical solution for *all* values of *Pe*. One technical reason is that our high-*Pe* approximation, $\sigma^{(\mathrm{hi})}$, is not the usual asymptotic series of singular perturbation, since we have essentially 'summed' parts of a naive expansion exactly in the Bessel function terms of (4.16). This allows the approximation to be more accurate than a simple power-series type of expansion, presumably extending its validity to somewhat higher *Pe*. Still, the neglected higher-order terms involve powers of *Pe*, which become important as *Pe* becomes small.

As we have mentioned throughout the paper, similarity solutions govern the asymptotic limits. For $Pe \to 0$, we are perturbing around the trivial similarity solution with uniform diffusive flux from infinity, $\sigma = \text{constant}$ and $c(r, \theta) \propto \ln r$. As shown in figure 4(*a*) for $Pe = 0.01$, a small amount of fluid flow changes this picture only

slightly near the disk, by favouring flux to one side compared to the other. When $Pe = 1$, as in figure 4(*b*), the region of depleted concentration begins to be swept significantly downstream by the flow. This causes the low-Pe approximation to break down near the rear stagnation point, while remaining fairly accurate near the forward stagnation point, as shown in figure 9.

The high-Pe approximation is derived by perturbing around a different similarity solution (2.17) for an absorbing circular rim on an absorbing flat plate (Bazant 2004). In this advection-dominated regime, there is a thin diffusion layer of width $O(1/\sqrt{Pe})$, around the disk, as shown in figure 4(*c*), which provides the first term in the approximation (5.24). The asymptotic corrections in § 4 are obtained by effectively removing the 'false plate' from the similarity solution, downstream from the disk.

To understand the influence of downstream perturbations, consider the Green's function (2.7), which has the asymptotic form

$$G(x, y) \sim \frac{\mathrm{e}^{Pe(x-r)}}{\sqrt{8\pi Pe\, r}} \quad \text{as } r = \sqrt{x^2 + y^2} \to \infty. \tag{7.1}$$

Green's function decays exponentially at the scale of Pe in all directions, except precisely downstream, where it is long-ranged: $G(x, 0) \sim 1/\sqrt{8\pi Pex}$ as $x \to \infty$ for $y = 0$. Therefore, all corrections to the leading-order similarity solution (2.17) decay exponentially upstream beyond an $O(Pe)$ distance from the rear stagnation point. Our high-Pe approximation, $\sigma^{(\mathrm{hi})}$, in (4.16) captures the first such correction, which is needed for uniform accuracy over the disk. Further corrections are $O(\mathrm{e}^{-4Pe})$, as is clear from formulae (4.23).

The fact that the approximation breaks down when e^{4Pe}, rather than Pe, gets close to unity explains the fortuitous accuracy of $\sigma^{(\mathrm{hi})}$ down to $Pe = 0.1$. Higher-order terms further extend the region of accuracy by orders of magnitude, e.g., to $Pe = O(10^{-3})$ for five terms, as shown in figure 7. Because the approximation is valid for a wide range of Pe that would not be considered 'high', it overlaps with the low-Pe approximation.

We also mention some directions for further analysis. The analytical treatment on the basis of an integral equation essentially avoids the complications of boundary-layer theory applied directly to the BVP (Hinch 1991). In that sense, it resembles renormalization-group (RG) methods for PDEs (Goldenfeld 1992; Chen, Goldenfeld & Oono 1996), which provide a general means of deriving asymptotic expansions in place of traditional problem-specific singular-perturbation methods. An attractive feature of RG methods is that they promise to produce globally valid approximations *directly*, without the need to combine distinct overlapping expansions, as we have done. It would be interesting to see if this could possibly be accomplished for our BVP, and, if so, whether the resulting approximations are any simpler or more accurate than ours. We leave this as an open challenge to RG aficionados.

From the point of view of mathematical methods, another interesting observation is that the BVP (1.3)–(1.5) can be formulated in analogous way to the problem of wave scattering by a finite strip (Myers 1965) in acoustics or electromagnetics, which has some variants with other geometries such as the scattering by a broken corner (Myers 1984). Such problems, where the requisite PDEs are or can be reduced to Helmholtz-type equations by simple transformations, can be described alternatively by finite sets of nonlinear ODEs in which the length of the strip, or the Péclet number Pe in the present case, is the independent variable. The underlying method is an improvement over Latta's method (Latta 1956) for the solution of a class of singular integral equations via their exact conversion to ODEs.

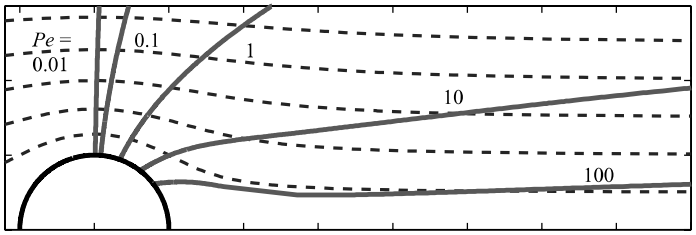

FIGURE 13. The locus of points, for various values of Pe (solid lines), where the concentration c attains its maximum along the streamlines (dashed lines) around a circular disk for desorption into an unconcentrated fluid. (In the equivalent problem of absorption from a concentrated fluid, the solid curves give the minimum concentration along streamlines for different Pe.)

Another technical question is how to place the method of high-Pe expansion pursued in § 4 on a more firm mathematical basis. To address this issue, two of us have developed an equivalent approach based on a generalization of the Wiener–Hopf technique applied to the BVP (1.3)–(1.5) in the Fourier domain, which yields the same results as the iteration scheme of § 4 (Margetis & Choi 2004). Since the Wiener–Hopf method is well known in this context for a semi-infinite strip (Carrier *et al.* 1983), it would be interesting to ask how the method might be extended for the present case of a finite strip, or perhaps more general situations, such as multiple strips, or three-dimensional objects.

A more careful comparison should be made of our numerical solutions with Kornev & Mukhamadullina (1994). Our method in § 3 seems to require more computational resources to obtain the same level of accuracy because it solves a two-dimensional BVP, whereas the other method solves a one-dimensional integral equation. Aspects of the technique in § 4.3 also need to be studied further, especially the number of the required terms versus Pe, the accuracy for $Pe \ll 1$ and the propagation of error through the requisite multiple integrals.

7.3. *Physical discussion*

Our analysis provides quantitative information about the crossover between diffusion-dominated and advection-dominated absorption, which is important in applications. As described above, the former regime, at low Pe, is characterized by a broad diffusion layer extending in all directions like a 'cloud', with the flow causing only a minor broken symmetry, as shown in figure 4(a). In contrast, at high Pe, concentration gradients are confined to a thin boundary layer around the object, which separates into a long thin 'wake' near the rear stagnation point, as shown in figure 4(c).

What is the critical Pe for the cloud-to-wake transition? Of course, the answer depends on one's definition, but the shape of the object also plays a role. In streamline coordinates, the transition is not so obvious since the object corresponds to an infinitely thin strip, which cannot 'shield' a thinner finite-sized wake. Objects of finite thickness, however, do show a clear transition. A uniformly valid formula for $c(x, y; Pe)$ in any geometry may be obtained by inserting our expression for the flux to the strip (6.1) into the convolution integral (2.8) and conformally mapping from the desired shape to the strip, $w = f(z)$.

The cloud-to-wake transition is related to $f(z)$, as we illustrate for the case of the disk, $f(z) = z + 1/z$. The analytical approximation is nearly indistinguishable from the numerical solution in figure 4, so we consider the latter. In figure 13, we show curves

where, for different values of Pe, the concentration change, relative to the background, is maximal along streamlines. Far from the disk, they approach parabolae, $Pe\, y^2 = 4x$, due to balance between diffusion in the y-direction scaling as $y \sim 2\sqrt{t}$ and advection in the x-direction scaling as $x \sim Pe\, t$. Near the object, the map causes a significant distortion of the curves, which allows us to define the critical value, $Pe = 60$, above which they become non-monotonic functions of x. At larger values of Pe, the curves are sucked back into a thinner wake region behind the disk, signifying the dominance of advection.

It is interesting to note the limiting wake structure as $Pe \to \infty$. As the concentration boundary layer wraps all the way around the disk, the downstream disturbance begins to look like that of a Green's function source located at the rear stagnation point. If one defines the 'wake' as the region behind the disk enclosed by a given iso-concentration line, $c = c_0$, then it is easy to see that the wake tends to a finite length as $Pe \to \infty$, even though its thickness tends to zero, like $1/\sqrt{Pe}$. Physically, the (dimensionless) length $L = O(l_0^2 Pe) = O(1)$ is the distance travelled in the flow downstream in x during the time for diffusion across the initial wake thickness, $l_0 = O(1/\sqrt{Pe})$. For example, the $c = 0.5$ contour ends roughly 2.3 disk diameters downstream from the rear stagnation point, as $Pe \to \infty$.

These results have relevance for more complicated physical situations, such as the coating of fibres from a gas flow, where quasi-steady advection–diffusion in a two-dimensional potential flow is a reasonable model for the growth dynamics (K. G. Kornev, private communication). It is well known that the Péclet number, based on the fibre diameter, controls the total growth rate, as well as the uniformity of the coating's thickness, for a single fibre. For $Pe \leqslant 0.1$, the flux to the disk (or fibre cross-section), $\sigma(\theta, Pe)$, is nearly uniform, apart from a minor asymmetry due to the flow, which is accurately described by (5.24). For $Pe \geqslant 0.01$, the high-Pe expansion (4.16) shows how the flux profile becomes increasingly asymmetric and approaches the advection-dominated limit, $\sigma \sim 2\sqrt{Pe/\pi}\, \sin\theta/2$ as $Pe \to \infty$. Our work provides an analytical description of how this crossover occurs for the flux profile (6.1), and the total flux (6.4), which may be useful in future analytical or numerical studies of the coating process.

By quantifying the crossover in the concentration field, we also provide some insight into the possible effect of interactions between multiple nearby fibres during real coating process. In the 'cloud' regime at low Pe, the concentration field approximately satisfies Laplace's equation, which means that other fibres in all directions can strongly influence the local flux, due to the long-range decay of the concentration. In the 'wake' regime at high Pe, the concentration remains uniform (outside a thin boundary layer) in all directions except directly downstream, where a thin wake forms of $O(1/\sqrt{Pe})$ thickness and $O(1)$ extent (at the scale of a few particle diameters). When the mean fibre spacing is larger than the typical wake length, there are negligible interactions, but, whenever a fibre ends up in the wake of another fibre, its coating becomes much thinner in a localized region, which can be undesirable. Our analysis shows that this important crossover occurs at a critical value of $Pe \approx 60$.

Another physical application of our results is to advection–diffusion-limited aggregation (Bazant *et al.* 2003), the stochastic analogue of the fibre coating problem, which involves discrete diffusing particles collecting on a seed in a potential flow. The ADLA model may have relevance for the dendritic growth of mineral oxide deposits in very thin cracks in rocks, where Hele-Shaw flow, laden with oxygen diffusing from the surface, is believed to occur over geological time scales (G. R. Rossman, private communication). To describe ADLA growth from a finite seed in a uniform

background flow, the probability measure for adding particles on a growing aggregate in the z-plane is given by the flux to the unit disk for the same problem in the w-plane,

$$p(z,t)|\mathrm{d}z| = p(\theta,t)\mathrm{d}\theta \propto \sigma_w(\theta;Pe(t)), \tag{7.2}$$

where the renormalized Péclet number, $Pe(t) = A_1(t)Pe_o$, is given by the time-dependent conformal radius. Our accurate numerical solution for $\sigma_w(\theta;Pe)$ has already been used as the growth measure in the simulations of Bazant *et al.* (2003). Future simulations or mathematical analysis could start from our nearly exact formula, $\sigma^{(\mathrm{conn})}$ from (6.1), which captures the full crossover between diffusion-dominated and advection-dominated dynamical fixed points with increasing $Pe(t)$.

T. M. S and M. Z. B would like to thank École Supérieure de Physique et Chimie Industrielles (Laboratoire de Physico-chimie Théorique) for hospitality and partial support. T. M. S. gratefully acknowledges an NSF Mathematical Sciences Postdoctoral fellowship and the Lee A. Dubridge Prize Postdoctoral fellowship from Caltech. The authors also wish to thank Konstantin Kornev, John Myers, Howard Stone, Jacob White, and Tai Tsun Wu for references and helpful discussions.

Appendix. Invertibility of the kernel

In this appendix we show that the symmetrized kernel, $K_0(Pe|x-x'|)$, of the integral equation (2.9) is positive definite. Using the relation

$$K_0(x) = \frac{1}{2}\int_{-\infty}^{\infty}\mathrm{d}t\ \frac{\cos(xt)}{\sqrt{1+t^2}}, \tag{A 1}$$

the kernel is recast into the form

$$\int_{-\infty}^{\infty}\mathrm{d}t\ \frac{\cos(\varsigma t)\cos(\varsigma_0 t)+\sin(\varsigma t)\sin(\varsigma_0 t)}{\sqrt{1+t^2}}. \tag{A 2}$$

It follows that, for $\beta > 0$,

$$\int_{-\beta}^{\beta}\mathrm{d}\varsigma_0\int_{-\beta}^{\beta}d\varsigma\ \int_{-\infty}^{\infty}\mathrm{d}t\ \frac{\cos(\varsigma t)\cos(\varsigma_0 t)+\sin(\varsigma t)\sin(\varsigma_0 t)}{\sqrt{1+t^2}}f(\varsigma_0)f(\varsigma)=\int_{-\infty}^{\infty}\mathrm{d}t\ \frac{g(t)^2+h(t)^2}{\sqrt{1+t^2}}, \tag{A 3}$$

by which the kernel is positive definite. The functions $g(t)$ and $h(t)$ are real, and given by

$$g(t)+\mathrm{i}h(t) = \int_{-\beta}^{\beta}f(u)\mathrm{e}^{\mathrm{i}ut}\,\mathrm{d}u. \tag{A 4}$$

REFERENCES

Acrivos, A. & Taylor, T. D. 1962 Heat mass transfer from single spheres in Stokes flow. *Phys. Fluids* **5**, 387–394.

Aleksandrov, V. M. & Belokon, A. V. 1967 Asymptotic solutions of a class of integral equations and its application to contact problems for cylindrical elastic bodies. *Prikl. Mat. Mekh.* **31**, 718–724.

Aleksandrov, V. M. & Belokon, A. V. 1968 Asymptotic solutions of a class of integral equations encountered in the investigation of mixed problems of the mathematical physics for regions with cylindrical boundaries. *Prikl. Mat. Mekh.* **32**, 402–413.

Aleksandrov, V. M. & Pozharskii, D. A. 1999 An asymptotic method in contact problems. *Prikl. Mat. Mekh.* **63**, 283–290.

ALIMOV, M. M., KORNEV, K. G. & MUKHAMADULLINA, G. L. 1994 The equilibrium shape of an ice-soil body formed by liquid flow past a pair of freezing columns. *Prikl. Mat. Mekh.* **58**, 873–888.

ALIMOV, M., KORNEV, K. & MUKHAMADULLINA, G. 1998 Hysteretic effects in the problems of artificial freezing. *SIAM J. Appl. Maths* **59**, 387–410.

BATEMAN MANUSCRIPT PROJECT 1981 *Higher Transcendental Functions*, Vol. II (ed. A. Erdélyi), p. 82. McGraw-Hill.

BATCHELOR, G. K. 1967 *An Introduction to Fluid Dynamics*. Cambridge University Press.

BAZANT, M. Z. 2004 Conformal mapping of some non-harmonic functions in transport theory. *Proc. R. Soc. Lond.* A **460**, 1433–1452.

BAZANT, M. Z., CHOI, J. & DAVIDOVITCH, B. 2003 Dynamics of conformal maps for a class of non-Laplacian growth phenomena. *Phys. Rev. Lett.* **91**, art. no. 045503.

BOUSSINESQ, M. J. 1905 Sur le pouvoir refroidissant d'un courant liquide ou gazeux. *J. de Math.* **1**, 285–290.

BRENNER, H. 1963 Forced convection heat and mass transfer at small Péclet numbers from a particle of arbitrary shape. *Chem. Engng Sci.* **18**, 109–122.

BURGERS, J. M. 1948 A mathematical model illustrating the theory of turbulence. *Adv. Appl. Mech.* **1**, 171–199.

CARLEMAN, T. 1922 Über die Abelsche Integralgleichung mit konstanten Integrationsgrenzen. *Math. Zeitschrift* **15**, 111–120.

CARRIER, G., KROOK, M. & PEARSON, C. E. 1983 *Functions of a Complex Variable*, Chaps. 2, 5 and 8. Ithaca, New York: Hod Books.

CHEN, L. Y., GOLDENFELD, N. D. & OONO, Y. 1996 The renormalization group and singular perturbations: multiple scales, boundary layers and reductive perturbation theory. *Phys. Rev.* E **54**, 376–394.

CHUGUNOV, V. A. & KORNEV, K. G. 1986 Dynamics of ice-rock barriers under conditions of freezing of filtering rocks. Inzh.-Fiz. Zh. **51**, 981–986.

CUMMINGS, L. M., HOHLOV, Y. E., HOWISON, S. D. & KORNEV, K. 1999 Two-dimensional solidification and melting in potential flows. *J. Fluid. Mech.* **378**, 1–18.

CUMMINGS, L. J. & KORNEV, K. 1999 Evolution of flat crystallisation front in forced hydrodynamic flow-some explicit solutions. *Physica* D **127**, 33–47.

EAMES, I. & BUSH, J. W. M. 1999 Long dispersion by bodies fixed in a potential flow. *Proc. R. Soc. Lond.* A **455**, 3665–3686.

GALIN, L. A. 1945 Unsteady filtration with a free surface. *Dokl. Acad. Nauk. SSSR* **47**, 246–249 (in Rusian).

GOLDENFELD, N. 1992 *Lectures on Phase Transitions and the Renormalization Group*. Reading, Massachusetts: Perseus Books.

GRADSHTEYN, I. S. & RYZHIK I. M. 1980 *Tables of Integrals, Series, and Products*. Academic.

HINCH, E. J. 1991 *Perturbation Methods*. Cambridge University Press.

HOWISON, S. D. 1992 Complex variable methods in Hele-Shaw moving boundary problems. *Eur. J. Appl. Maths* **3**, 209–224.

HUNT, J. C. R. & EAMES, I. 2002 The disappearance of laminar and turbulent wakes in complex flows. *J. Fluid Mech.* **457**, 111–132.

KOPLIK, J., REDNER, S. & HINCH, E. J. 1994 Tracer dispersion in planar multipole flows. *Phys. Rev.* E **50**, 4650–4667.

KORNEV, K. G. & CHUGUNOV, V. A. 1988 Determination of the equilibrium shape of the bodies formed during the solidification of filteration flow. *Prikl. Mat. Mekh.* **52**, 773–778.

KORNEV, K. & MUKHAMADULLINA, G. 1994 Mathematical theory of freezing for flow in porous media. *Proc. R. Soc. Lond.* A **447**, 281–297.

KREIN, M. G. 1962 Integral equations on a half line with kernel depending upon the difference of the arguments. *Am. Math. Transl.* **22**, 163–288.

LATTA, G. E. 1956 The solution of a class of integral equations. *Rat. Mech. Anal.* **5**, 821–831.

LEAL, G. 1992 *Laminar Flow and Convective Transport Processes*. Butterworth-Heineman.

MAGAR, V., GOTO, T. & PEDLEY, T. J. 2003 Nutrient uptake by a self-propelled steady squirmer. *Q. J. Mech. Appl. Maths* **56**, 65–91.

MAKSIMOV, V. A. 1976 On the determination of the shape of bodies formed by solidification of the fluid phase of the stream. *Prikl. Mat. Mekh.* **40**, 264–272.

MARGETIS, D. & CHOI, J. 2005 Iteration scheme by the Wiener–Hopf method for a class of first-kind integral equations. *Stud. Appl. Maths* (submitted).

MOREGA, M. & BEJAN, A. 1994 Heatline visualization of forced convection in porous media. *Intl J. Heat Fluid Flow* **36**, 42–47.

MUSKHELISHVILI, N. I. 1992 *Singular Integral Equations.* Dover (based on the second Russian edition of 1946).

MYERS, J. M. 1965 Wave scattering and the geometry of a strip. *J. Math. Phys.* **6**, 1839–1846.

MYERS, J. M. 1984 Derivation of a matrix Painlevé equation germane to wave scattering by a broken corner. *Physica* D **11**, 51–89.

NOBLE, B. 1988 *Methods based on the Wiener-Hopf Technique for the Solution of Partial Differential Equations,* 2nd Edn. New York: Chelsea.

PEARSON, C. E. 1957 On the finite strip problem. *Quart. Appl. Math.* **XV**, 203–208.

PHILLIPS, C. G. 1990 Heat and mass transfer from a film into steady shear flow. *Q. J. Mech. Appl. Maths* **43**, 135–159.

POLUBARINOVA-KOCHINA, P. YA. 1945 On a problem of the motion of the contour of a petroleum shell. *Dokl. Akad. Nauk. SSSR* **47**, 254–257 (in Russian).

PROTSENKO, V. S. & RVACHEV, V. L. 1976 Plate in the form of an infinite strip on an elastic half-space. *Prikl. Mat. Mekh.* **40**, 273–280.

RVACHEV, V. L. 1956 The pressure on an elastic half-space of a stamp in the form of a strip in a plane. *Prikl. Mat. Mekh.* **20**, 163–179 (In Russian).

STAKGOLD, I. 1998 *Green's Functions and Boundary Value Problems,* 2nd Edn. Wiley.

TITCHMARSH, E. C. 1948 *Introduction to the Theory of Fourier Integrals,* 3rd Edn. Clarendon.

TREFETHEN, L. N. 1986 *Numerical Conformal Mapping.* North Holland.

TREFETHEN, L. N. 2000 *Spectral Methods in Matlab.* Philadelphia: Society for Industrial and Applied Mathematics.

VAN WIJNGAARDEN, L. 1966 Asymptotic solution of a diffusion problem with mixed boundary conditions. *Proc. Koninkl. Nederl. Akad. Wet.* **69**, 263–276.